VOLUME 8 NUMBER 3-4 2021 ISSN 2409-6121; eISSN 2522-1361

Physical Sciences and Technology

National Nanotechnological Laboratory of Open Type
Institute of Experimental and Theoretical Physics

Physical Sciences and Technology is publishing two number in a year by al-Farabi Kazakh National University, al-Farabi ave., 71, 050040, Almaty, the Republic of Kazakhstan
website: http://phst.kaznu.kz/

Any inquiry for subscriptions should be send to:
Gauhar Mussabek, al-Farabi Kazakh National University
al-Farabi ave., 71, 050040, Almaty, the Republic of Kazakhstan
e-mail: gauharmussabek@gmail.com

SCOPE AND AIM

Physical Sciences and Technology provides an original paperback for the publication of peerreviewed research and review articles in all fields of Physics and related Technology. The topics, included in the scope, especially emphasize understanding of the physics underlying modern technology.

Subject areas may include, but are not limited to the following fields: Astronomy and Space Research, Theoretical Physics and Astrophysics, Plasma Physics and Related Technology, Chemical Physics and Related Technology, Condensed Matter Physics and Related Technology, Thermal physics and Related Technology, Nuclear Physics and Related Technology, Nanomaterials and Nanotechnology, Applied Atomic and Molecular Physics, Material Sciences and Related Technology, Electronics and Related Technology, Instrumentation, Photonics and Quantum Electronics, Signal processing.

The Journal is issued under the auspices of the National Nanotechnological Laboratory of Open Type and Institute of Experimental and Theoretical Physics and is published two times a year by the «Kazakh University» Publishing House. The International Editorial Board of the Journal consists of leading researchers from different countries of the world. The Journal is wide open for contributions that both lie at the far frontiers of contemporary physics and are particularly aimed at applications of the scientific principles of physics to modern technological problems.

IRSTI 34.49.23 https://doi.org/10.26577/phst.2021.v8.i2.01

Estimated measurements of natural background radiation in the surface atmospheric layer of the Almaty region

V.V. Dyachkov*, M.T. Bigeldiyeva, Yu.A. Zaripova and A.V. Yushkov

Al-Farabi Kazakh National University, Almaty, Kazakhstan
e-mail:*lnirp206@gmail.com

The radon isotopes of natural radioactive radiation of the earth's crust emanating to the surface are concentrated in the human environment and have a direct impact on the people health. Due to this fact the problem of studying the radiation distributions in the surface atmospheric layer of the Earth is urgent. In this work, measurements of the exposure dose rate, beta particle flux, and equivalent equilibrium volumetric activity (EEVA) of radon in the surface atmospheric layer of the Earth have been performed. Measurements of radon and gamma, beta backgrounds were carried out from April 2021 to August 2021 in the Almaty region at various altitudes above sea level: from 500 to 2500 meters. They were carried out using electronic radiometric equipment: beta-dosimeter "RKS-01B-SOLO"; gamma dosimeter "RKS-01G-SOLO"; radiometer of radon-222 "RAMON-02" in the field. As a result, preliminary assessment schemes were built for route measurements of the 222Rn radon isotope, beta and gamma radiation fields from natural daughter products of decay of radon isotopes and radionuclides located in the surface atmospheric layer. As a result of this work, an altitude dependence of changes in the natural radiation gamma and beta background of the surface surface layer is presented, which grows with an increase in the surface above sea level. The different activity of radon over rocks and soils is shown, which, as is known, is associated with the exhalation of radon and which depends, among other things, on the density of the soils. The preliminary results of measurements of significant perturbations of the EEVA of radon did not reveal.

Key words: variations in time of radon; natural beta active radionuclides; coagulation; atmospheric radioactive nanoparticles.
PACS number: 23.60.

1 Introduction

The territory of Kazakhstan is characterized by a complex radiation situation due to the presence of active mine development of rich deposits of minerals, especially coal, non-ferrous metals and uranium, geological features, seismically active zones in the south and mountainous areas. Radon and its decay products, which are formed in natural radioactive chains, have a significant effect on the general background radiation among natural sources of ionizing radiation. The radionuclides formed during such decays, from the depths of the lithosphere, by coagulation and further diffusion, enter the surface atmospheric layer [1-4]. The contribution of radon to the average annual radiation dose from natural sources is more than 50%. Due to the fact that radon isotopes are concentrated in the human environment and have a direct impact on the health of the population, the problem of studying the distributions of radon isotopes emanations in the surface atmospheric layer of the Earth remains relevant.

The concentration of radon and its daughter decay products (DDP) in the surface atmospheric layer is extremely uneven and depends on the geological and geophysical characteristics of the natural environment [5], in this regard, different countries use their own approaches to determining the radon hazard of the territory. At present, all countries are striving to carry out radiation-ecological measurements and research on the radon hazard, which are based on methods for mapping radon. So, in the countries of the European Union, the concept of «geogenic radon potential» is key in assessing the potential radon hazard of territories [6-9]. At the same time, in different countries, the concept is based on various factors: in Serbia – the content of natural radionuclide in the soil [10], in Norway – the correlation between indoor radon and geology [11], in Switzerland – the dose rate of gamma radiation, geology, lines faults, permeability of the upper soil layer [12].

The natural background radiation in the regions of Kazakhstan averages 3.1 mSv/year [13]. And the total dose from natural and man-made sources of radiation on average per person in Kazakhstan is about 4 mSv/year, which is one and a half times higher than the world average. The study of the spatial distribution of the emanation of radon isotopes in the foothill Almaty region of the Tien Shan is an urgent task, since tectonic faults and mountain fallows are additional sources of radiation of radon and its daughter decay products. The purpose of this study was to perform preliminary assessment measurements of the radiation hazard for the population exposed to alpha, beta, gamma radiation at the level of the surface atmospheric layer from the daytime surface of the Earth.

2 Experimental procedure and methodology

In this work, field measurements of gamma and beta radiation fields on the surface of the earth's layer were carried out and the concentration of radon in suspended aerosol particles in the surface atmospheric layer was measured. Methods for performing measurements were worked out according to [14-16] and optimized for the given field measurements. The difficulties in performing the experimental part of this work are related to the fact that measurements had to be carried out under certain meteorological conditions, since their influence rather strongly causes fluctuations in the exhalation of radon from the soil into the atmosphere [17]. In addition, carry out measurements during this season to avoid the influence of seasonal variations in the measured data [18-19]. The control points for measuring gamma-fan, beta-background and radon activity were chosen for reasons of minimal changes in external factors (depressions, pits of natural origin). Humidity and temperature were monitored at these points.

Measurements of the spatial distribution of radon isotopes were carried out from April 2021 to August 2021 with dry soil and stable meteorological conditions in the foothills of the Trans-Ili Alatau Tien Shan in the Almaty region at various altitudes above sea level: from 500 to 2500 meters. In connection with the developed comprehensive urban planning scheme for the territory of the Almaty region until 2045, the study area was selected and located in the foothill Almaty region on an area of 4500 km^2: its coordinates are between 43.20–43.85 ° north latitude and 76.32–77, 50 ° east longitude. Measurements of the natural radiation near-surface layer of the earth were carried out using electronic radiometric equipment: a radiometer beta-dosimeter "RKS-01B-SOLO"; gamma dosimeter "RKS-01G-SOLO"; concentration of radon in suspended aerosol particles in the surface atmospheric layer – with a radon radiometer "RAMON-02". All measurement results were performed with a statistical error not exceeding 10% (at each control point, from 3 to 5 measurements were carried out).

3 Analysis of experimental data

As a result of field measurements, preliminary estimation schemes of the route of control points for measuring gamma background, beta background (Fig. 1, 2) and a scheme of the route of control points (Fig. 3) for measuring the equivalent equilibrium volumetric activity of radon (EEVA) were built. In Table 1, the geolocation coordinates of the positions of the control measuring points and the corresponding values of the beta-particles flux, the exposure dose rate (EDR) and the EEVA of radon, taking into account the instrumental error, for the RKS-01B-SOLO beta dosimeter – 15%; gamma dosimeter "RKS-01G-SOLO" – 12% and radon radiometer "RAMON-02" – 30%.

Figures 1-2 and 4-5 show that the altitude dependence of changes in the natural radiation gamma and beta background of the surface surface layer manifests itself quite well. Despite the local fluctuations of values from the general growing trend, this effect is confidently recorded. In addition to natural beta radionuclides of terrestrial origin, such as 40K and 87Rb, the DDP of radon isotopes, which are also the DDP of thorium, uranium-radium and uranium-actinium series of natural terrestrial chains of radioactive decay [20- 22]. As you know, in the foothills of rocks, radon exhalation is low through dense rocks (not taking into account local cracks in rocks due to their inhomogeneous spatial distribution), and also, as you know, in porous soils, radon exhalation is high, which is indirectly, of course necessary. at the same time, making corrections for horizontal transfer, mixing of air masses of the surface layer is reflected in the scheme of the route of control points for measuring the EEVA of radon (Figure 3). Of course, the rate of dissolution and mixing in the surface atmospheric layer must be taken into account for future measurements. In this work, this parameter was taken into account qualitatively, by choosing a place for measurements.

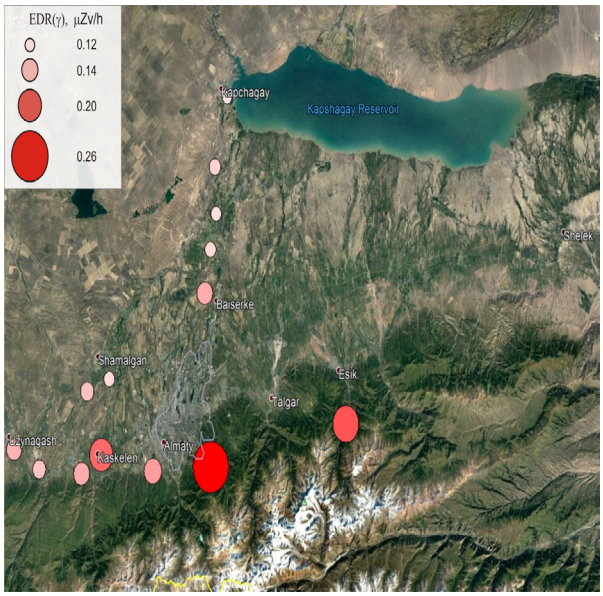

Figure 1 – Scheme of the route of control points for measuring the natural radiation gamma background of the surface layer.

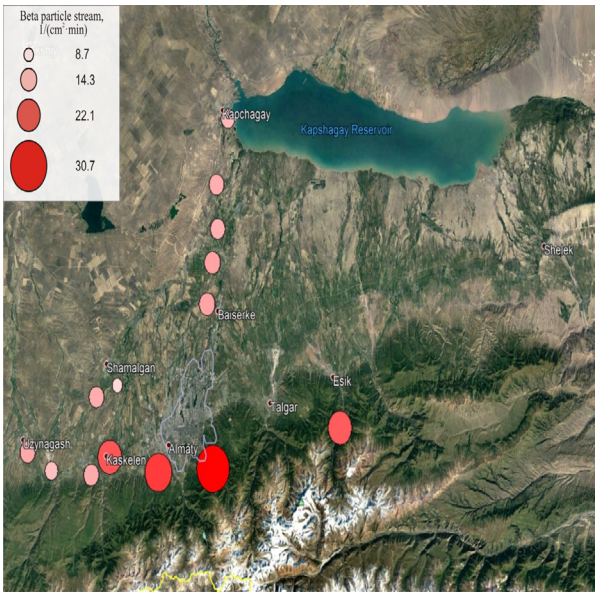

Figure 2 – Scheme of the route of control points for measuring the natural radiation beta background of the surface layer.

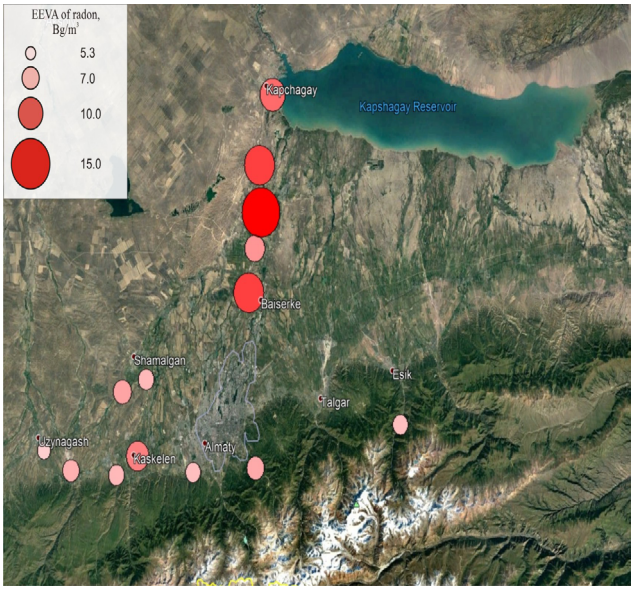

Figure 3 – Scheme of the route of control points for measuring the equivalent equilibrium volumetric activity of the 222Rn radon isotope.

Table 1 – The values of the geolocation coordinates of the positions of the control measuring points and the corresponding values of the flux of beta particles, EDR and EEVA of radon.

Pos.	Latitude, degrees	Longitude, degrees	Altitude, m	EDR(g	Beta particle stream, 1/(cm²·min)	EEVA (^{222}Rn), Bq/m³
1	43.1695000	76.8137100	1013	0.168±0.020	25.0±3.7	6.0±1.8
2	43.2552980	77.4836280	1722	0.211±0.025	21.5±3.2	6.0±1.8
3	43.1780920	77.0163810	1273	0.264±0.031	30.7±4.6	7.0±2.1

Table continuation

Pos.	Latitude, degrees	Longitude, degrees	Altitude, m	EDR(g	Beta particle stream, 1/(cm^2·min)	EEVA (^{222}Rn), Bq/m^3
4	43.4930300	76.9939700	601	0.158±0.019	14.2±2.1	12.0±3.6
5	43.5728200	77.0136000	567	0.132±0.016	14.3±2.1	8.0±2.4
6	43.6378800	77.0337800	533	0.128±0.015	13.0±1.9	15.0±4.5
7	43.7232600	77.0293300	500	0.136±0.016	13.2±2.0	12.0±3.6
8	43.8507100	77.0722600	481	0.124±0.015	12.1±1.8	10.0±3.0
9	43.1983085	76.6333545	843	0.198±0.024	22.1±3.3	9.0±2.7
10	43.1639867	76.5653418	970	0.159±0.019	13.4±2.0	6.3±1.9
11	43.1711225	76.4172858	993	0.144±0.017	11.4±1.7	6.7±2.0
12	43.2065420	76.3282000	837	0.155±0.019	13.7±2.1	5.3±1.6
13	43.3135819	76.5831044	729	0.146±0.017	13.3±2.0	7.3±2.2
14	43.3363474	76.6603148	702	0.131±0.016	8.7±1.3	6.3±1.9

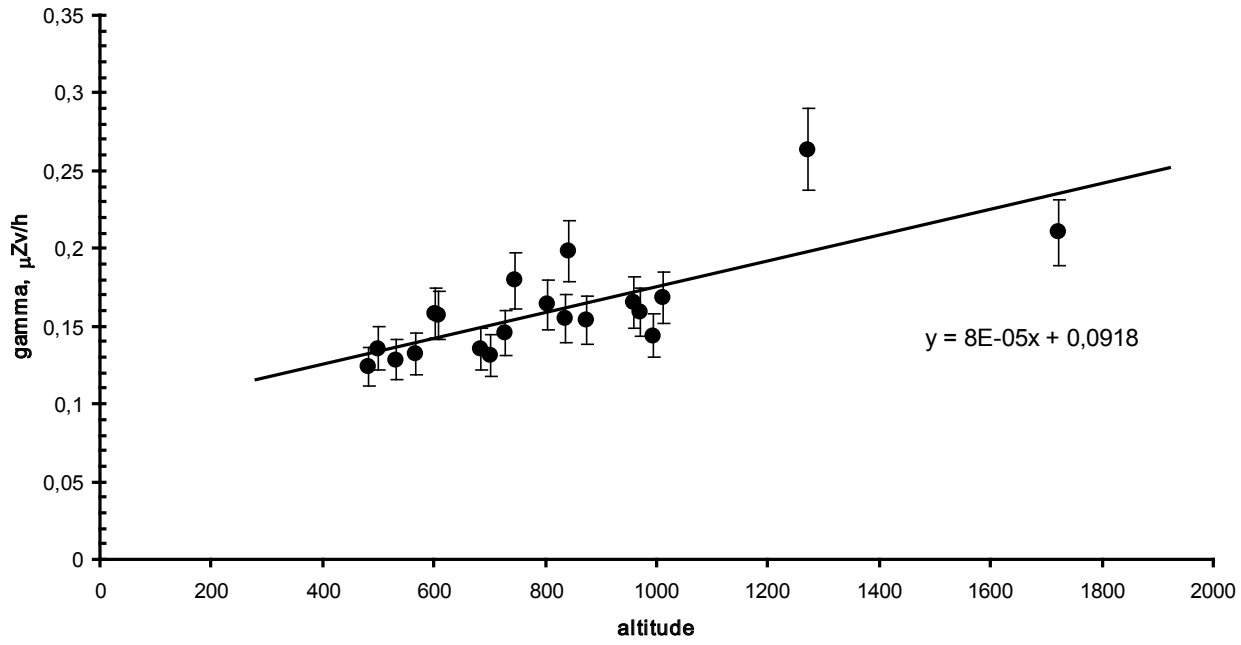

Figure 4 – Dependence of the natural radiation gamma background of the surface layer on the height above sea level (altitude).

In this work, the values of the beta background are in satisfactory agreement and correlate with the results of beta-spectrometry of samples of the surface layer of soil taken in different places in Almaty [23-24]. EEVA of radon does not obey such a clear relationship. The concentration of radon in suspended aerosol particles in the surface atmospheric layer is quite sensitive to the local geological structure (groundwater, soil type and its porosity) and meteorological conditions. But, nevertheless, as expected, you can notice different radon activity over rocks and soils. The averaged values as a whole over the entire measurement range are in good agreement with the results obtained in [25].

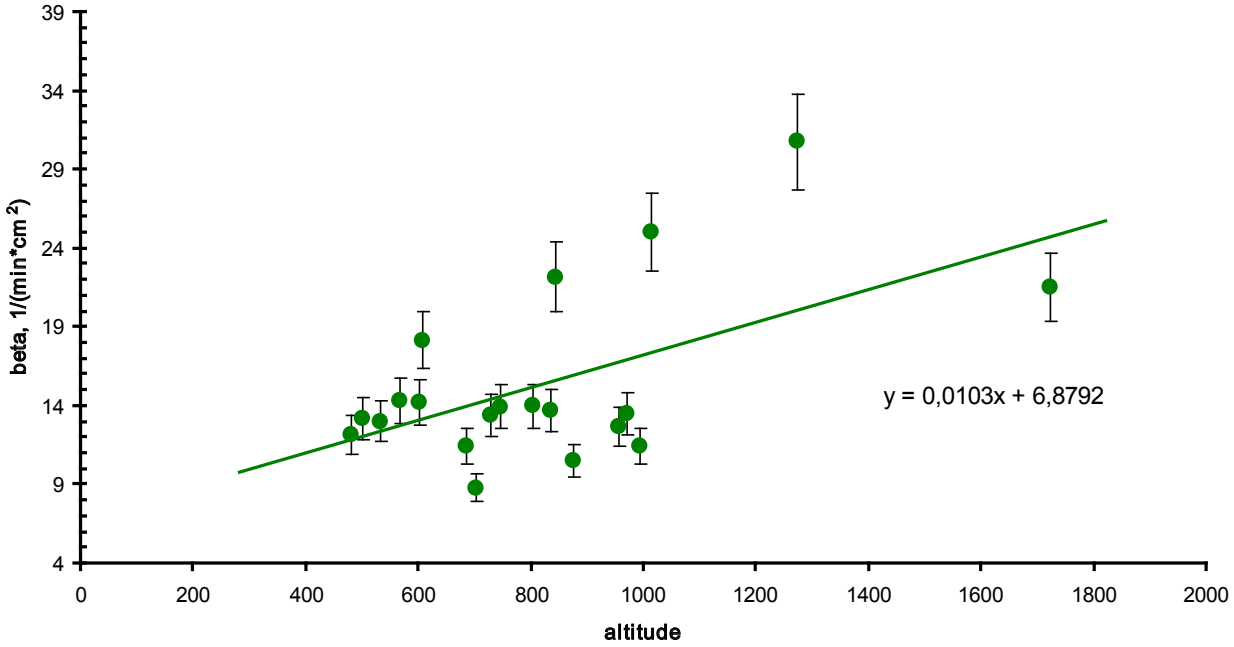

Figure 5 – Dependence of the natural radiation beta background of the surface layer on the height above sea level (altitude)

4 Conclusions

Thus, as a result of route measurements of gamma and beta radiation fields on the surface of the earth's layer and the concentration of radon in suspended aerosol particles in the surface atmospheric layer, preliminary estimation schemes of route measurements of the distribution of natural radiation gamma and beta background of the surface layer and a route measurement scheme were constructed distribution of the equivalent equilibrium volumetric activity of the radon isotope. An altitude dependence of changes in the natural radiation gamma and beta background of the surface layer is shown, which grows with an increase in the surface above sea level. The different activity of radon over rocks and soils is shown, which, as is known, is associated with the exhalation of radon and which depends, among other things, on the density of the soils. The preliminary results of measurements of significant perturbations of the EEVA of radon did not reveal.

Aknowledgements

This research is funded by the Science Committee of the Ministry of Education and Science of the Republic of Kazakhstan (Grant No. AP09258978).

References

1 V. S. Yakovleva, V. D. Karataev. Criteria for assessing the potential radon hazard of territories // Radiation biology. Radioecology –2004. –Vol. 44. –No.2 –Pp. 227–231 (in Russian).

2 V. S. Yakovleva, V. D. Karataev, A. V. Vukolov, I. I. Ippolitov, M. V. Kabanov, P. M. Nagorskiy, S. V. Smirnov, P. P. Firstov, R. I. Parovik. Methodology of a multifactorial experiment on radon transport processes in the "lithosphere-atmosphere" system // ANRI. -2009. –No. 4. –Pp. 55-60 (in Russian).

3 P. M. Nagorskiy, I. I. Ippolitov, S. V. Smirnov, V. S. Yakovleva, V. D. Karataev, A. V. Vukolov, V. V. Zukau. Features of monitoring of radioactivity in the "lithosphere-atmosphere" system by β- and γ-radiation // Izvestiya VUZov. Physics. –2010. – Vol.53. – No.11. –Pp. 55-59 (in Russian).

4 V. S. Yakovleva, P. M. Nagorskiy, M. S. Cherepnev. Formation of a-, b- and g-fields of the surface atmosphere by natural atmospheric radionuclides // Bulletin KRAUNZ. Phys.-mat. Science. –2014. –Vol. 1. – No. 8. – Pp. 86-96 (in Russian).

5 M. Garcia-Talavera, A. Garcia-Perez, C. Rey, I. Ramos. Mapping radon prone areas using γ-radiation dose rate and geological information // Journal of Radiological Protection. – 2013. –Vol. 33. –No.3. – Pp. 605–20. https://doi.org/10.1088/0952-4746/33/3/605.

6 C. Sabbarese, F. Ambrosino, A. D'Onofrio, M. Pugliese, G. La Verde, V. D'Avino, V. Roca. The first radon potential map of the Campania region (southern Italy) // Applied Geochemistry. –2021. –Vol. 126. – Pp. 104890. https://doi.org/10.1016/j.apgeochem.2021.104890

7 S. N. Manohar, H. A. J. Meijer, M. A. Herber. Radon flux maps for the Netherlands and Europe using terrestrial gamma radiation derived from soil radionuclides // Atmospheric Environment. –2013. –Vol. 81. – Pp. 399-412. https://doi.org/10.1016/j.atmosenv.2013.09.005

8 G. Ielsch, M. E. Cushing, Ph. Combes, M. Cuney. Mapping of the geogenic radon potential in France to improve radon risk management: methodology and first application to region Bourgogne // Journal of Environmental Radioactivity. –2010. –Vol. 101. –No. 10. – Pp. 813-820. https://doi.org/10.1016/j.jenvrad.2010.04.006

9 F. Giustini, G. Ciotoli, A. Rinaldini, L.Ruggiero, M. Voltaggio. Mapping the geogenic radon potential and radon risk by using Empirical Bayesian Kriging regression: A case study from a volcanic area of central Italy // Science of The Total Environment. –2019. –Vol. 661. – Pp. 449-464. https://doi.org/10.1016/j.scitotenv.2019.01.146

10 M. E. Savkovic, V. Udovicic, D. Maletic, G. Pantelic, P. Ujic, I. Celikovic, S. Forkapic, V. Markovic, V. Arsic, J. Ilic, B. Markoski. Results of the first national indoor radon survey performed in Serbia // Journal of Radiological Protection. – 2020. –Vol. 40. –No.2. https://doi.org/10.1088/1361-6498/ab749e

11 R. J.Watson, M. A.Smethurst, G. V.Ganerod, I. Finne, A. Liv Rudjord. The use of mapped geology as a predictor of radon potential in Norway // Journal of Environmental Radioactivity. –2017. –Vol. 166. –No. 2. – Pp. 341-354. https://doi.org/10.1016/j.jenvrad.2016.05.031

12 G. Kropat, F. Bochud, Ch. Murith, M. Palacios (Gruson), S. Baechler. Modeling of geogenic radon in Switzerland based on ordered logistic regression // Journal of Environmental Radioactivity. –2017. –Vol. 166. –No. 2. – Pp. 376-381. https://doi.org/10.1016/j.jenvrad.2016.06.007

13 R. I. Bersimbaev, O. Bulgakova. The health effects of radon and uranium on the population of Kazakhstan // Genes and Environment. –2015. –Vol. 37. –No. 18. https://doi.org/10.1186/s41021-015-0019-3

14 V. S. Yakovleva. Analysis of methods for measuring the flux density of radon and thoron from the earth's surface // Equipment and news of radiation measurements. –2010. –No. 3. –Pp. 23-30 (in Russian).

15 V. S. Yakovleva. Methods for measuring the flux density of radon and thoron from the surface of porous materials, Publishing house of the Tomsk Polytechnic University, Tomsk, 2011, 174 p. (in Russian).

16 V. I. Zherebchevsky, N. A. Maltsev. Measurement of the content of radon and thoron in samples, Publishing House BBM, Saint Petersburg, 2020, 38p. (in Russian).

17 T. I. Sisigina. Oscillations of radon exhalation from soil to atmosphere due to changes in meteorological conditions, Radioactivity of the atmosphere, soil, and fresh waters // Proceedings of the Institute of Experimental Meteorology, Moscow Department of Hydrometeorological Publishing House, Moscow, -1970. -Pp. 3–15. (in Russian).

18 V. V. Dyachkov, Z. M. Biyasheva, A. A. Komarov, Yu. A. Zaripova, A. L. Shakirov, A. V. Yushkov, O. Kh. Hamdieva, V. A. Sysoev. Experimental detection of four-day variations in radon emanation caused by the phases of the Moon // KazNU Bulletin. Physical series. –2016. – No. 1 (56) .– Pp. 120-128. (in Russian).

19 V.V. Dyachkov, S. T. Alibekov, Yu.A. Zaripova, A. V. Yushkov. Spatial and temporal patterns of radon distribution, Kazakh University Publishing House, Almaty, 2019, 101 p. (in Russian).

20 E. A. Klementyeva, S. V. Ovsyannikova, A. N. Nikitin. Dynamics of 210-Pb and 210-Po isotopes in natural meadow ecosystems and agrophytocenoses with regular application of phosphorus fertilizers // Proceedings of the National academy of sciences of Belarus. Biological series. –2017. –No. 1. –Pp. 39–47. (in Russian).

21 S. V. Druzhinin. Isotopes beryllium-7, polonium-210, lead-210 in atmospheric precipitation and aerosols in Arkhangelsk // Bulletin Pomor. university. Ser .: Natural. science. –2010. –No. 4. –Pp. 15-19. (in Russian).

22 T. Zalewska, D. Biernacik, M. Marosz. Correlations between 7Be, 210Pb, dust and PM10 concentrations in relation to meteorological conditions in northern Poland in 1998–2018 // Journal of Environmental Radioactivity. –2021. –Vol. 228. https://doi.org/10.1016/j.jenvrad.2020.106526

23 V. V. Dyachkov, Yu. A. Zaripova, A. V. Yushkov, A. L. Shakirov, M. T. Bigeldiyeva, K. S. Dyussebayeva, K. E. Abramov. Periodic variations in time of atmospheric radioactive nanoparticles // Physical sciences and technology. –2019. –Vol. 6. –No. 1-2. –Pp. 11-17. https://doi.org/10.26577/phst-2019-1-p6

24 V. V. Dyachkov, Yu. A. Zaripova, A. V. Yushkov, A. L. Shakirov, Z. M. Biyasheva, M. T. Bigeldiyeva, K. S. Dyussebayeva, K. E. Abramov. A study of the accumulation factor of the daughter products of radon decay in the surface layer using beta spectrometry // Physics of Atomic Nuclei. –2018. –Vol. 81. – Pp. 1509 – 1514. https://doi.org/10.1134/S106377881811008X

25 G. V. Fyodorov, P. G. Kayukov, G. D. Berkinbaev. Radioecology of Kazakhstan // Materials of IV International conferences, Tomsk. –2013. – Pp. 542-545. (in Russian).

IRSTI 29.15.17 https://doi.org/10.26577/phst.2021.v8.i2.02

Analytical determination of the non-relativistic quantum mechanical properties of near doubly magic nuclei

E. A. Thompson*, E. P. Inyang and E. S. William

Theoretical Physics Group, Department of Physics, University of Calabar, Calabar, Nigeria
*e-mail:edyy7000@yahoo.com

A non-relativistic analytical study of some atomic nuclei near doubly-magic nuclei, namely 41Ca and 41Sc. These nuclei under study are considered to have a closed core with a single nucleon orbiting the core, thus agreeing perfectly with the nuclear shell model. The superposition of Hulthen potential plus Spin – orbit interaction plus adjusted Coulomb is used as the nucleon – nucleon potential for this study. This superposition forms a suitable potential model useful in describing the net force mediating the interactions between nucleons in a nuclear system. The combined potentials effectively represent three basic interactions within the nucleus. By employing the Nikiforov – Uvarov method of solving the Schrodinger equation, we have calculated the energy eigenvalues and the eigen function of these nuclei. Also, the expectation values for radius, kinetic energy and momentum of each nucleus under study are also evaluated analytically. The results obtained are in agreement with experiment. As such, the constructed potential model used in the present work is recommended for similar nuclei.

Key words: Schrödinger equation, Hulthen potential, spin-orbit interaction, Coulomb potential, energy eigenvalues eigenfunction, expectation values.

1 Introduction

The atomic nuclei are an intricate quantum mechanical system. The study of its structure, which boarders on how its constituent particles and nucleons are arranged, is key to understanding and interpreting certain observations displayed by bulk matter. The atomic nucleus is made up of protons and neutrons that are arranged in a predictable order within the nuclear volume. [1-2]. A clear insight into the structure of the nuclear system, which is the core of nuclear properties research, coupled with our understanding of inter-nucleon forces, can be explored and used to critically test both our knowledge of the nuclear forces and many-body theories [3-4].

The shell model and the single – particle energies offer a veritable ground for study and understanding basic features and properties of atomic nuclei [5-8]. The single-particle energies obtained using the nuclear shell model are expected to be influenced by the nuclear spin-orbit force [9]. However, the shell model is aptly applicable to closed shells with a lone valence-nucleon nuclei [10]. Most importantly, the single-particle behaviour is observed in near magic and near doubly magic nuclei, where the major shells are filled up with nucleons in a nucleus, leaving a single proton or neutron to occupy the next shell after a major or minor gap. For instance, ^{41}Ca and ^{41}Sc are modelled as doubly magic nuclei with a single particle orbiting the $1f_{\frac{7}{2}}$level. The shell model predicts that the properties of a nucleus are correctly represented by the properties of the lone nucleon orbiting the core, taking the pairing effect into consideration [11]. As such, a valence proton orbiting the N = Z =20 core for the ^{41}Sc isotope and a valence neutron orbiting the N = Z = 20 core for the ^{41}Ca are used to predict to a large extent accurately the properties of these nuclei.

In this study, we have constructed a nuclear potential model within the non-relativistic domain of quantum mechanics which takes into consideration the basic interactions taking place within the atomic nucleus. These interactions include the strong interaction represented in our model by the Hulthen potential, the spin-orbit interaction represented here by the spin-orbit potential and the electromagnetic interaction

represented in our model by the Coulomb potential. By the superposition of these three potential models, we have been able to model the forces mediating the basic interactions within the nucleus. As such, our constructed potential model is suitably applied to the Schrodinger wave equation to obtain the energy eigenvalues, wave function and other quantum mechanical observables for the nucleus.

The Hulthen potential is a central mean field potential used to present a short-ranged force field. In this research, the Hulthen represents the strong force which influence the interaction between nucleons inside the nucleus. In the present study, the Hulthen potential is the nucleon – nucleon (N-N) potential. The spin-orbit interaction is a vital component of the force field under which nucleons interacts [12]. The spin-orbit effect arises from the interaction of the nucleon magnetic moment with the mean field potential. This effect is usually visible for orbits with $\ell \geq 0$ [13]. Hence, coupling the spin-orbit interaction to the mean field potential for nucleon – nucleon interaction is of essence. In relativistic quantum mechanics, the spin is effectively represented in the wave equation (Dirac equation) describing the motion of a spin ½ particle [14]. Although the non-relativistic Schrodinger wave equation does not consider the spin of a particle rightly, in this study the spin has been factored in by introducing the spin-orbit interaction into the N-N potential. This has been done successfully in this work, as is presented in the subsequent sections. Interactions between the core, which contains the positively charged proton, and the orbiting valence proton necessitate the introduction of the adjusted Coulomb potential.

In this study, the non-relativistic nuclear shell model is used to obtain analytically the single particle ground state energies for ^{41}Ca and ^{41}Sc, near doubly magic nuclei. To achieve this aim, we solved analytically the Schrodinger equation for a constructed potential model formed by the superposition of the Hulthen potential [15] plus spin-orbit potential plus the adjusted Coulomb potential [16] as an effective potential between the core and a single particle. These potentials are important nuclear potentials used in describing the interaction between a single nucleon and the nuclear core. [17-20]. However, the adjusted Coulomb potential strength is set to zero in the case where the single particle orbiting the core is a neutron. Furthermore, the Hellman-Feynman theorem is used to obtain some physical observables such as radii, kinetic energies, and momenta for the nuclei under study.

Now that the choice of the N-N potential has been made, the next step is to solve the Schrodinger wave equation. We use the Nikiforov-Uvarov (NU) method to solve the Schrodinger equation [21]. The organization of this paper is as follows: The NU method is reviewed in section 2; the non-relativistic energy spectrum is presented in section 3; expectation values of physical observables are stated in section 4, and results and discussion are presented in section 5.

2 Review of the NU method

We introduce the NU method briefly in this section; details can be obtained from ref. [21]. This method is based on solving the second order differential equation of the hyper geometric type:

$$\psi^{||}(z) + \frac{\tilde{\tau}(z)}{\sigma(z)}\psi^{|}(z) + \frac{\tilde{\sigma}(z)}{\sigma^2(z)}\psi(z) = 0 \qquad (1)$$

In Eq. (1), $\sigma(z)$ and $\tilde{\sigma}(z)$ are polynomials of at most second degree. $\tilde{\tau}(z)$ is a first-degree polynomial, and $\psi(z)$is the hypergeometric-type function, $\psi^{||}(z)$ and $\psi^{|}(z)$are the second and the first order derivative of the hypergeometric- type function with respect to the spatial coordinates respectively. A possible solution to Eq. (1) is proposed as

$$\psi(z) = \phi(z)y(z) \qquad (2)$$

The function y (z) which is the second part of the proposed solution given by Eq. (2) can be obtained from the equation below;

$$\sigma(z)y^{||}(z) + \tau(z)y^{|}(z) + \lambda y(z) = 0 \qquad (3)$$

Equation (3) is the hypergoemetric type second order differential equation obtained from the relationship between the polynomials $\sigma(z)$ and $\tilde{\tau}(z)$, details of this relationship can be obtained from Nikiforov and Uvarov ref. [21].

From Eq. (2), the function $\phi(z)$ is the solution of a differential equation of the form given by:

$$\sigma(z)\phi^{|}(z) - \pi(z)\phi(z) = 0 \qquad (4)$$

where

$$\tau(z) = \check{\tau}(z) + 2\pi(z) \qquad (5)$$

and λ in Eq. (3) is a parameter defined as

$$\lambda = \lambda_n = -n\tau^{|}(z) + \frac{n(n-1)}{2}\sigma^{|\ |}(z) = \\ = 0(n = 0,1,2,3,\dots) \quad (6)$$

The function $\tau(z)$ is a polynomial in terms of z, and to obtain a proper solution, its first derivative $\tau^{|}(z)$ must be negative. The function $y(z)$ as stated in Eq. (2) is the hyper geometric type wave function obtained by using the Rodrigues relation:

$$y_n(z) = \frac{B_n(z)d^n}{\rho(z)dz^n}[\sigma^n(z)\rho(z)] \quad (7)$$

where B_n is a constant related to normalization, and the weighted function $\rho(z)$ is defined as:

$$\frac{d}{dz}[\sigma(z)\rho(z)] = \tau(z)\rho(z) \quad (8)$$

Also, the function $\pi(z)$ which is a first-degree polynomial is defined as

$$\pi(z) = \frac{\sigma^{|}(z) - \tilde{\tau}(z)}{2} \pm \\ \pm\sqrt{\left(\frac{\sigma^{|}(z)-\tilde{\tau}(z)}{2}\right)^2 - \tilde{\sigma}(z) + k\sigma(z)} \quad (9)$$

k in Eq. (9) is related to the parameter λ Eq. (6), and the first derivative of $\pi^{|}(z)$ as

$$\lambda = k + \pi^{|}(z) \quad (10)$$

The value of k is obtained by equating the discriminant of the quadratic expression under the square root sign in Eq. (10) to zero, and solving the resulting equation for k. By solving Eq. (6) and Eq. (10), we derive the energy eigenvalue equation.

3 Solution of Schrodinger equation for Hulthen potential plus spin-orbit interaction plus adjusted Coulomb potential

The eigenvalues of the energy E for nuclei is obtained by solving the radial component of the 3-dimensional Schrodinger wave equation given as

$$\frac{d^2R(r)}{dr^2} + \frac{2}{r}\frac{dR(r)}{dr} + \\ + \frac{2\mu}{\hbar^2}\left[E_{n\ell j} - V_{eff}(r)\right]R(r) = 0 \quad (11)$$

This equation is for a single particle, where μ is the reduced mass of a single nucleon, $E_{n\ell j}$ is the energy spectrum, V_{eff} is our constructed potential model which has in it the centrifugal term, $\hbar$ is the Planck's constant, n, ℓ and j are the principal, orbital and total momentum quantum number respectively. By transforming the variable from $r \to z$, let a new variable be defined as

$$z = e^{-\alpha r} \quad (12)$$

The derivatives of the function $R(r)$ in Eq. (11) are obtained in terms of the new variable z, as such Eq. (11) is transformed and restated in terms of z as $R(r)$ is redefined as $\psi(z)$.

By transforming Eq. (11) using the new variable defined by Eq. (12), the Schrodinger equation becomes as stated below

$$\frac{d^2\psi(z)}{dz^2} + \frac{1}{z}\frac{d\psi(z)}{dz} + \frac{1}{\alpha^2 z^2}\left[\frac{2\mu E}{\hbar^2} - \frac{2\mu}{\hbar^2}\left(V_{eff}\right)\right] = 0 \quad (13)$$

The central potential in this case is the Hulthen potential which is an approximation of the well-known Woods Saxon potential. This potential has been successfully used to approximate the nuclear central force:

$$V_H(r) = -\frac{V_o\alpha e^{-\alpha r}}{1-e^{-\alpha r}} \quad (14)$$

where V_o in Eq. (14) is the potential strength of the Hulthen potential.

The adjusted Coulomb potential is given as

$$V_c(r) = \frac{e^2}{R_o}\left[3 - \left(\frac{r}{R_o}\right)^2\right] \quad (15)$$

where e is the charge of e^- or proton, R_0 the radius of nuclei and r is the range of this position of a particle from the core. The spin-orbit interaction is given as

$$V_{LS}(r) = \frac{1}{2}V_{LS}(0)\left(\frac{r_o}{\hbar}\right)^2\frac{1}{r}\left[\frac{dV_H(r)}{dr}\right]\overrightarrow{L.S} \quad (16)$$

where $\vec{L}.\vec{S} = \frac{\hbar^2}{2}\left(j(j+1) - \ell(\ell+1) - \frac{3}{4}\right)$.

The centrifugal term of the Schrodinger wave equation is given as

$$V_{cf} = \frac{\hbar^2}{2\mu}\frac{\ell(\ell+1)}{r^2} \quad (17)$$

The effective potential V_{eff} for the nuclei system is obtained by summing up Eq. (14), Eq. (15), Eq. (16) and Eq. (17) as given by Eq. (18):

$$V_{eff} = -\frac{V_o e^{-\alpha r}}{1-e^{-\alpha r}} - V_{LS}(0) r_o^2 \frac{1}{r} \frac{\alpha e^{-\alpha r}}{(1-e^{-\alpha r})^2} \vec{L}.\vec{S} - \frac{3e^2}{\pi\varepsilon_0 R_o} + \frac{e^2 r^2}{\pi\varepsilon_0 R_o^3} + \frac{\hbar^2}{2\mu}\frac{\ell(\ell+1)}{r^2} \quad (18)$$

We apply the Greene-Aldrich approximations scheme [22], [23], [24] to handle the centrifugal barrier. The approximation is valid for $\alpha \ll 1$. It is of the following forms:

$$\frac{1}{r^2} \approx \frac{4\alpha^2 e^{-2\alpha r}}{(1-e^{-2\alpha r})^2} \quad (19)$$

$$\frac{1}{r^2} \approx \frac{\alpha^2}{(1-e^{-2\alpha r})^2} \quad (20)$$

The approximations stated in Eq. (19) and Eq. (20) are commonly used in calculations, but in the present work Eq. (20) is used, as this particular approximation scheme suit our purpose. Applying the Greener-Aldrich approximation scheme as stated by Eq. (20) to solve the Schrodinger equation makes our solution an approximate solution. An exact solution can only the attempted for our constructed potential if ℓ=0, but this will cancel the spin-orbit effect from the results. Putting Eq. (18), Eq. (19) and Eq. (20) into Eq. (13), the Schrodinger equation now reads:

$$\frac{d^2\psi(z)}{dz^2} + \frac{1}{z}\frac{d\psi(z)}{dz} + \frac{1}{z^2(1-z)^2}\begin{bmatrix} \frac{2\mu E}{\hbar^2\alpha^2}(1-z)^2 + V_o\frac{2\mu}{\hbar^2\alpha^2}z(1-z) \\ +V_{LS}(0)\frac{2\mu r_o^2}{\hbar^2}\left(\frac{z}{1-z}\right)\left(j(j+1)-\ell(\ell+1)-\frac{3}{4}\right) \\ -\frac{6\mu e^2}{R_o\pi\varepsilon_0\alpha^2\hbar^2}(1-z)^2 + \frac{2\mu e^2}{\hbar^2\pi\varepsilon_0\alpha^4 R_o^3}(1-z)^4 \\ -\ell(\ell+1)z \end{bmatrix}\psi(z) = 0 \quad (21)$$

By applying the principles suggested by [25] into the higher powers of z beyond the second degree, Eq. (21) is transformed to the hyper geometric-type second order differential equation solvable by the NU method:

$$\frac{d^2\psi(z)}{dz^2} + \frac{(1-z)}{z(1-z)}\frac{d\psi(z)}{dz} + \frac{1}{z^2(1-z)^2}\begin{bmatrix} -\frac{2\mu E}{\hbar^2\alpha^2}z^2 + V_{LS}(0)\frac{2\mu r_o^2}{\hbar^2}\left(j(j+1)-\ell(\ell+1)-\frac{3}{4}\right)z^2 \\ -\frac{6\mu e^2}{R_o\pi\varepsilon_0\alpha^2\hbar^2}z^2 + 6\frac{2\mu e^2}{\hbar^2\pi\varepsilon_0\alpha^4 R_o^3}z^2 - V_o\frac{2\mu}{\hbar^2\alpha}z^2 \\ +2\frac{2\mu E}{\hbar^2\alpha^2}z + V_{LS}(0)\frac{2\mu r_o^2}{\hbar^2}\left(j(j+1)-\ell(\ell+1)-\frac{3}{4}\right)z \\ +2\frac{6\mu e^2}{R_o\pi\varepsilon_0\alpha^2\hbar^2}z - 4\frac{2\mu e^2}{\hbar^2\pi\varepsilon_0\alpha^4 R_o^3}z - \ell(\ell+1)z \\ +V_o\frac{2\mu}{\hbar^2\alpha}z - \frac{2\mu E}{\hbar^2\alpha^2} - \frac{6\mu e^2}{R_o\pi\varepsilon_0\alpha^2\hbar^2} + \frac{2\mu e^2}{\hbar^2\pi\varepsilon_0\alpha^4 R_o^3} \end{bmatrix}\psi(z) = 0 \quad (22)$$

where

$$\varphi = \begin{Bmatrix} -\frac{2\mu E}{\hbar^2\alpha^2} + V_{LS}(0)\frac{2\mu r_o^2}{\hbar^2}\left(j(j+1)-\ell(\ell+1)-\frac{3}{4}\right) \\ -\frac{6\mu e^2}{R_o\pi\varepsilon_0\alpha^2\hbar^2} + 6\frac{2\mu e^2}{\hbar^2\pi\varepsilon_0\alpha^4 R_o^3} - V_o\frac{2\mu}{\hbar^2\alpha} \end{Bmatrix} \quad (23)$$

$$\eta = \begin{Bmatrix} 2\frac{2\mu E}{\hbar^2\alpha^2} + V_{LS}(0)\frac{2\mu r_o^2}{\hbar^2}\left(j(j+1)-\ell(\ell+1)-\frac{3}{4}\right) \\ +2\frac{6\mu e^2}{R_o\pi\varepsilon_0\alpha^2\hbar^2} - 4\frac{2\mu e^2}{\hbar^2\pi\varepsilon_0\alpha^4 R_o^3} + V_o\frac{2\mu}{\hbar^2\alpha} - \ell(\ell+1) \end{Bmatrix} \quad (24)$$

$$-\Re = \frac{2\mu E}{\hbar^2\alpha^2} + \frac{6\mu e^2}{R_o\pi\varepsilon_0\alpha^2\hbar^2} - \frac{2\mu e^2}{\hbar^2\pi\varepsilon_0\alpha^4 R_o^3} \quad (25)$$

Substituting equations (23), (24) and (25) into Eq. (22), we have:

$$\frac{d^2\psi(z)}{dz^2} + \frac{(1-z)}{z(1-z)}\frac{d\psi(z)}{dz} + \\ + \frac{1}{z^2(1-z)^2}[\varphi z^2 + \eta z - \Re]\psi(z) = 0 \quad (26)$$

Comparing (26) and (1), the relevant polynomials can be expressed as

$$\tilde{\tau}(z) = 1 - z,$$

$$\sigma(z) = z(1-z), \qquad \sigma^2(z) = z^2(1-z)^2$$

$$\tilde{\sigma}(z) = \varphi z^2 + \eta z - \Re \quad (27)$$

Inserting the polynomials as defined by Eq. (27) into Eq. (9), we have:

$$\pi(z) = \frac{-z}{2} \pm \sqrt{(\gamma - k)z^2 + (\eta + k)z + \Re} \quad (28)$$

where

$$\gamma = \frac{1}{4} + \varphi \quad (29)$$

As required by the NU method the discriminant of the quadratic expression under the square root sign in Eq. (28) is equated to zero. This leads to another quadratic equation in terms of k. Solving the ensuing quadratic equation for k, we have possible solutions as:

$$k = -(\eta + 2\Re) \pm 2\sqrt{\Re}\sqrt{\gamma + \eta + \Re} \quad (30)$$

Accepting the negative solution of k from Eq. (30), and substituting k into Eq. (28), we have

$$\pi(z) = \frac{-z}{2} \pm \left(\sqrt{\Re} + \sqrt{\gamma + \eta + \Re}\right)z - \sqrt{\Re} \quad (31)$$

Upon inserting Eq. (31) into Eq. (5) another required polynomial τ(z) is derived:

$$\tau(z) = 1 - 2z - \\ -2\left(\sqrt{\Re} + \sqrt{\gamma + \eta + \Re}\right)z - 2\sqrt{\Re} \quad (32)$$

Taking the first derivative of Eq. (32), we have:

$$\tau^{|}(z) = -2 - 2\sqrt{\Re} - 2\sqrt{\gamma + \eta + \Re} \quad (33)$$

Taking the first derivative of Eq. (31) and using Eq. (30), Eq. (33) as well as Eq. (27), λ and λ_n are obtained explicitly as

$$\lambda = \frac{-1}{2} - \sqrt{\Re} - \sqrt{\gamma + \eta + \Re} - \\ -\eta - 2\Re - 2\sqrt{\Re}\sqrt{\gamma + \eta + \Re} \quad (34)$$

$$\lambda_n = n^2 + n + 2n\sqrt{\Re} + 2n\sqrt{\gamma + \eta + \Re} \quad (35)$$

By comparing Eq. (34) and Eq. (35), we obtain the quantity$\Re$:

$$\Re = \left[\frac{-\frac{1}{2}\left[\left(n+\frac{1}{2}+\sqrt{\beta}\right)^2 + \frac{1}{4} + \xi\right]}{\left(n+\frac{1}{2}+\sqrt{\beta}\right)}\right]^2 \quad (36)$$

where

$$\beta = \gamma + \eta + \Re$$
$$\xi = -\frac{1}{4} - \gamma + \Re \quad (37)$$

Reintroducing Eq. (23), Eq. (24) and Eq. (25) into Eq. (37) and Eq. (36), we obtain the energy eigenvalues for the superposition Hulthen potential, spin-orbit interaction and adjusted Coulomb potential in terms of the principal n, orbital ℓ and angular momentum j quantum numbers as stated by Eq. (38):

$$E_{n\ell j}=\frac{3e^2}{\pi\varepsilon_0 R_o}-\frac{e^2}{\pi\varepsilon_0\alpha^4 R_o^3}-\frac{\hbar^2\alpha^2}{8\mu}\left[\begin{array}{l}-\dfrac{\left[\left(n+\frac{1}{2}+\sqrt{\frac{1}{4}-\frac{4\mu V_{LS}(0)r_o^2}{\hbar^2}\left(j(j+1)-\ell(\ell+1)-\frac{3}{4}\right)-\frac{6\mu e^2}{\hbar^2\pi\varepsilon_0\alpha^4 R_o^3}+\ell(\ell+1)}\right)^2\right]}{\left(n+\frac{1}{2}+\sqrt{\frac{1}{4}-\frac{4\mu V_{LS}(0)r_o^2}{\hbar^2}\left(j(j+1)-\ell(\ell+1)-\frac{3}{4}\right)-\frac{6\mu e^2}{\hbar^2\pi\varepsilon_0\alpha^4 R_o^3}+\ell(\ell+1)}\right)}\\ +\dfrac{-\frac{2\mu V_o}{\hbar^2\alpha}+\frac{2\mu V_{LS}(0)r_o^2}{\hbar^2}\left(j(j+1)-\ell(\ell+1)-\frac{3}{4}\right)+\frac{10\mu e^2}{\hbar^2\pi\varepsilon_0\alpha^4 R_o^3}}{\left(n+\frac{1}{2}+\sqrt{\frac{1}{4}-\frac{4\mu V_{LS}(0)r_o^2}{\hbar^2}\left(j(j+1)-\ell(\ell+1)-\frac{3}{4}\right)-\frac{6\mu e^2}{\hbar^2\pi\varepsilon_0\alpha^4 R_o^3}+\ell(\ell+1)}\right)}\end{array}\right]^2 \quad (38)$$

Equation (38) is the energy eigenvalue equation for the proton orbiting the core in a nucleus. The energy spectrum for a neutron orbiting the core of the nucleus is obtained by setting e in Eq. (38) to zero as the net charge of the neutron is zero, as there is no Coulomb interaction between the orbiting neutron and the core of the nucleus. Hence the energy eigenvalues for the neutron is given as:

$$E_{n\ell j}=-\frac{\hbar^2\alpha^2}{8\mu}\left[\begin{array}{l}-\dfrac{\left[\left(n+\frac{1}{2}+\sqrt{\frac{1}{4}-\frac{4\mu V_{LS}(0)r_o^2}{\hbar^2}\left(j(j+1)-\ell(\ell+1)-\frac{3}{4}\right)+\ell(\ell+1)}\right)^2\right]}{\left(n+\frac{1}{2}+\sqrt{\frac{1}{4}-\frac{4\mu V_{LS}(0)r_o^2}{\hbar^2}\left(j(j+1)-\ell(\ell+1)-\frac{3}{4}\right)+\ell(\ell+1)}\right)}\\ +\dfrac{-\frac{2\mu V_o}{\hbar^2\alpha}+\frac{2\mu V_{LS}(0)r_o^2}{\hbar^2}\left(j(j+1)-\ell(\ell+1)-\frac{3}{4}\right)}{\left(n+\frac{1}{2}+\sqrt{\frac{1}{4}-\frac{4\mu V_{LS}(0)r_o^2}{\hbar^2}\left(j(j+1)-\ell(\ell+1)-\frac{3}{4}\right)+\ell(\ell+1)}\right)}\end{array}\right]^2 \quad (39)$$

Equation (38) and Eq. (39) are used in this study to obtain explicitly the ground state energy of ^{41}Sc and ^{41}Ca respectively.

Next, we obtain the wave function as stated in Eq. (8), using the weighted factor $\rho(z)$ which is in the form

$$\rho(z)=z^{2\sqrt{\Re}}.(1-z)^{2\sqrt{\gamma+\eta+\Re}} \quad (40)$$

Substituting Eq. (40) into Eq. (7), the Rodrigues relation is obtained as:

$$y_n(z)=B_n z^{-2\sqrt{\Re}}(1-z)^{-2\sqrt{\gamma+\eta+\Re}}\frac{d^n}{dz^n}\left[z^{n+2\sqrt{\Re}}(1-z)^{n+2\sqrt{\gamma+\eta+\Re}}\right]\equiv$$
$$\equiv P_n^{\left(2\sqrt{\Re},2\sqrt{\gamma+\eta+\Re}\right)}(1-2z) \quad (41)$$

where P_n is the Jacobi polynomial. Using Eq. (36) and Eq. (41) the wave function is given as:

$$\psi(z) = N_{n\ell} z^{\sqrt{\Re}}(1 - -z)^{\left(\frac{1}{2}+\sqrt{\gamma+\eta+\Re}\right)} P_n^{\left(2\sqrt{\Re},2\sqrt{\gamma+\eta+\Re}\right)}(1-2z) \quad (42)$$

where $N_{n\ell}$is the normalization constant. Applying the normalization condition the normalization constant is obtained as:

$$\frac{N_{n\ell}^2}{\alpha}\int_{-1}^{1}\left(\frac{1-y}{2}\right)^{\omega}\left(\frac{1+y}{2}\right)^{b}\left[P_n^{(\omega,b-1)}y\right]^2 dy = 1 \quad (43)$$

Equation (43) is derived by setting

$$b = \frac{1}{2} + \sqrt{\gamma+\eta+\Re}$$
$$\omega = 2\sqrt{\Re} \quad (44)$$

By comparing Eq. (43) to the standard integral of the form Eq. (37) as reported by Ebomwonyi et at., in the ref. [24], we have:

$$\int_{-1}^{1}\left(\frac{1-p}{2}\right)^{x}\left(\frac{1+p}{2}\right)^{y}\left[P_n^{(2x,2y-1)}y\right]^2 dp = = \frac{2\Gamma(x+n+1)\Gamma(y+n+1)}{n!x\Gamma(x+y+n+1)} \quad (45)$$

We derive the normalization constant as:

$$N_{n\ell} = \left[\frac{\alpha n!\omega\Gamma(\omega+b+n+1)}{2\Gamma(\omega+n+1)\Gamma(b+n+1)}\right]^{\frac{1}{2}} \quad (46)$$

4 Expectation values of some physical observables

Now we derive the expectation values for position (radius), kinetic energy and the square of momentum for the respective nuclei under study. To achieve this, we use the Hellmann-Feynman theorem. 'The Hellmann-Feynman theorem assures that a non-degenerate eigenvalue of a hermitian operator in a parameter dependent eigensystem varies with respect to the parameter provided that the associated normalized eigenfunction is continuous with respect to the parameter' [26]. This statement is given mathematically as:

$$\left\langle \psi_{\mathrm{q}} \left| \frac{\partial \mathrm{H}}{\partial \mathrm{q}} \right| \psi_{\mathrm{q}} \right\rangle = \frac{\partial \mathrm{E}}{\partial \mathrm{q}} \quad (47)$$

The Hamiltonian used in solving the Schrodinger equation for the present work is of the form:

$$H = -\frac{\hbar^2}{2\mu}\frac{d^2}{dr^2} - -\frac{\hbar^2}{\mu r}\frac{d}{dr} + \frac{\hbar^2}{2\mu r^2}\ell(\ell+1) - -\frac{V_o e^{-\alpha r}}{1-e^{-\alpha r}} - -V_{LS}(0)\frac{r_o^2\alpha e^{-\alpha r}}{(1-e^{-\alpha r})^3}\vec{L}.\vec{S} \quad (48)$$

To obtain the expectation value for position of the particle in the nuclear system, which represent approximately the radius of the nuclei under study, we equate the variable q in Eq. (47) to ℓ. Substituting Eq. (48) into Eq. (47), we have:

$$\langle\psi(\ell)|\frac{\partial H}{\partial \ell}|\psi(\ell)\rangle = \frac{\hbar^2}{2\mu}(2\ell+1)\langle r^{-2}\rangle \quad (49)$$

where $\langle r^{-2}\rangle$ is the expectation value for position (radius of the system).

Taking the derivative of Eq. (39) with respect to ℓ as required by Eq. (47), we have:

$$\frac{\partial E}{\partial \ell} = \left[-2AZ\left[(2\ell+1)\left(\frac{4\mu V_{\ell S} r_o^2}{\hbar^2}+1\right)\right]\cdot \left\{\frac{1}{2\sqrt{y}} - \frac{\frac{1}{2\sqrt{y}}\left(\frac{2\mu V_0}{\hbar^2\alpha}+\frac{2\mu V_{\ell S} r_o^2}{\hbar^2}\left(j(j+1)-\ell(\ell+1)-\frac{3}{4}\right)+\frac{10\mu e^2}{\hbar^2\pi\varepsilon_o\alpha^2 R_o^3}\right)}{\left(n+\frac{1}{2}+\sqrt{y}\right)^2}\right\}\right] \quad (50)$$

Equating (49) and (50), the expectation value for position is derived as:

$$\langle r^{-2}\rangle = \left[\begin{array}{l} -\frac{\alpha^2}{2}\left(n+\frac{1}{2}+\sqrt{y}+\frac{\frac{2\mu V_0}{\hbar^2\alpha}+\frac{2\mu V_{\ell S} r_o^2}{\hbar^2}\left(j(j+1)-\ell(\ell+1)-\frac{3}{4}\right)+\frac{10\mu e^2}{\hbar^2\pi\varepsilon_o\alpha^2 R_o^3}}{\left(n+\frac{1}{2}+\sqrt{y}\right)}\right). \\ \left\{\frac{1}{2\sqrt{y}}-\frac{\frac{1}{2\sqrt{y}}\left(\frac{2\mu V_0}{\hbar^2\alpha}+\frac{2\mu V_{\ell S} r_o^2}{\hbar^2}\left(j(j+1)-\ell(\ell+1)-\frac{3}{4}\right)+\frac{10\mu e^2}{\hbar^2\pi\varepsilon_o\alpha^2 R_o^3}\right)}{\left(n+\frac{1}{2}+\sqrt{y}\right)^2}\right\} \\ \left(\frac{4\mu V_{\ell S} r_o^2}{\hbar^2}+1\right) \end{array}\right] \quad (51)$$

The expectation value for position (radius) $\langle r\rangle$is obtained from Eq. (51). The expectation value for kinetic energy $\langle T\rangle$is obtained from Eq. (47) by setting

q to μ, and differentiating the Hamiltonian and the energy spectrum with respect to the reduced mass μ respectively. We have the derivatives below:

$$\frac{\partial H}{\partial \mu} = -\frac{1}{\mu}\left(-\frac{\hbar^2}{2\mu}\frac{d}{dr^2}-\frac{\hbar^2}{\mu r}\frac{d}{dr}+\frac{\hbar^2}{2\mu r^2}\ell(\ell+1)\right) \quad (52)$$

Recall that,

$$H = T + V$$
$$T = H - V \quad (53)$$

where T is the kinetic energy and V the potential, putting Eq. (53) into Eq. (52) we have:

$$\langle\psi(\mu)|\frac{\partial H}{\partial \mu}|\psi(\mu)\rangle = -\frac{1}{\mu}(H-V) = -\frac{1}{\mu}\langle T\rangle \quad (54)$$

Also,

$$\frac{\partial E}{\partial \mu} = \left[\begin{array}{l} \frac{\hbar^2\alpha^2}{8\mu^2}\left[n+\frac{1}{2}+\sqrt{y}+\frac{\frac{2\mu V_0}{\hbar^2\alpha}+\frac{2\mu V_{\ell S} r_o^2}{\hbar^2}\left(j(j+1)-\ell(\ell+1)-\frac{3}{4}\right)+\frac{10\mu e^2}{\hbar^2\pi\varepsilon_o\alpha^2 R_o^3}}{\left(n+\frac{1}{2}+\sqrt{y}\right)}\right]^2 \\ -\frac{\hbar^2\alpha^2}{4\mu}\left[n+\frac{1}{2}+\sqrt{y}+\frac{\frac{2\mu V_0}{\hbar^2\alpha}+\frac{2\mu V_{\ell S} r_o^2}{\hbar^2}\left(j(j+1)-\ell(\ell+1)-\frac{3}{4}\right)+\frac{10\mu e^2}{\hbar^2\pi\varepsilon_o\alpha^2 R_o^3}}{\left(n+\frac{1}{2}+\sqrt{y}\right)}\right]. \\ \left\{\frac{1}{2\sqrt{y}}\left[\left(-\frac{4V_{\ell S} r_o^2}{\hbar^2}\left(j(j+1)-\ell(\ell+1)-\frac{3}{4}\right)-\frac{6e^2}{\hbar^2\pi\varepsilon_o\alpha^4 R_o^3}\right)+1\right]+\right. \\ \left(\frac{\frac{2V_0}{\hbar^2\alpha}+\frac{2V_{\ell S} r_o^2}{\hbar^2}\left(j(j+1)-\ell(\ell+1)-\frac{3}{4}\right)+\frac{10e^2}{\hbar^2\pi\varepsilon_o\alpha^2 R_o^3}}{\left(n+\frac{1}{2}+\sqrt{y}\right)}\right) \\ -\frac{1}{2\sqrt{y}}\left(\frac{\frac{2\mu V_0}{\hbar^2\alpha}+\frac{2\mu V_{\ell S} r_o^2}{\hbar^2}\left(j(j+1)-\ell(\ell+1)-\frac{3}{4}\right)+\frac{10\mu e^2}{\hbar^2\pi\varepsilon_o\alpha^2 R_o^3}}{\left(n+\frac{1}{2}+\sqrt{y}\right)^2}\right) \\ \left.-\frac{\left(-\frac{4V_{\ell S} r_o^2}{\hbar^2}\left(j(j+1)-\ell(\ell+1)-\frac{3}{4}\right)-\frac{6e^2}{\hbar^2\pi\varepsilon_o\alpha^4 R_o^3}\right)}{\left(n+\frac{1}{2}+\sqrt{y}\right)^2}\right\} \end{array}\right] \quad (55)$$

Equating (54) and (55) as required by (47), and we obtain the expectation value for kinetic energy as:

$$\langle T\rangle = \left[\begin{array}{l} \frac{\hbar^2\alpha^2}{8\mu}\left[n+\frac{1}{2}+\sqrt{y}+\frac{\frac{2\mu V_0}{\hbar^2\alpha}+\frac{2\mu V_{\ell S}r_o^2}{\hbar^2}\left(j(j+1)-\ell(\ell+1)-\frac{3}{4}\right)+\frac{10\mu e^2}{\hbar^2\pi\varepsilon_o\alpha^2R_o^3}}{\left(n+\frac{1}{2}+\sqrt{y}\right)}\right]^2 \\ -\frac{\hbar^2\alpha^2}{4}\left[n+\frac{1}{2}+\sqrt{y}+\frac{\frac{2\mu V_0}{\hbar^2\alpha}+\frac{2\mu V_{\ell S}r_o^2}{\hbar^2}\left(j(j+1)-\ell(\ell+1)-\frac{3}{4}\right)+\frac{10\mu e^2}{\hbar^2\pi\varepsilon_o\alpha^2R_o^3}}{\left(n+\frac{1}{2}+\sqrt{y}\right)}\right]. \\ \left\{\frac{1}{2\sqrt{y}}\left[\left(-\frac{4V_{\ell S}r_o^2}{\hbar^2}\left(j(j+1)-\ell(\ell+1)-\frac{3}{4}\right)-\frac{6e^2}{\hbar^2\pi\varepsilon_o\alpha^4R_o^3}\right)+1\right]+\right. \\ \left(\frac{\frac{2V_0}{\hbar^2\alpha}+\frac{2V_{\ell S}r_o^2}{\hbar^2}\left(j(j+1)-\ell(\ell+1)-\frac{3}{4}\right)+\frac{10e^2}{\hbar^2\pi\varepsilon_o\alpha^2R_o^3}}{\left(n+\frac{1}{2}+\sqrt{y}\right)}\right) \\ -\frac{1}{2\sqrt{y}}\left(\frac{\frac{2\mu V_0}{\hbar^2\alpha}+\frac{2\mu V_{\ell S}r_o^2}{\hbar^2}\left(j(j+1)-\ell(\ell+1)-\frac{3}{4}\right)+\frac{10\mu e^2}{\hbar^2\pi\varepsilon_o\alpha^2R_o^3}}{\left(n+\frac{1}{2}+\sqrt{y}\right)^2}\right) \\ \left.-\frac{\left(-\frac{4V_{\ell S}r_o^2}{\hbar^2}\left(j(j+1)-\ell(\ell+1)-\frac{3}{4}\right)-\frac{6e^2}{\hbar^2\pi\varepsilon_o\alpha^4R_o^3}\right)}{\left(n+\frac{1}{2}+\sqrt{y}\right)^2}\right\} \end{array}\right] \quad (56)$$

Using the relationship between kinetic energy and the square of momentum as:

$$-\frac{1}{\mu}\langle T\rangle = -\frac{1}{2\mu^2}\langle P^2\rangle \quad (57)$$

The square of momentum is obtained from Eq. (57) as stated below:

$$\langle P^2\rangle = \left[\begin{array}{l} \frac{\hbar^2\alpha^2}{4}\left[n+\frac{1}{2}+\sqrt{y}+\frac{\frac{2\mu V_0}{\hbar^2\alpha}+\frac{2\mu V_{\ell S}r_o^2}{\hbar^2}\left(j(j+1)-\ell(\ell+1)-\frac{3}{4}\right)+\frac{10\mu e^2}{\hbar^2\pi\varepsilon_o\alpha^2R_o^3}}{\left(n+\frac{1}{2}+\sqrt{y}\right)}\right]^2 \\ -\frac{\mu\hbar^2\alpha^2}{2}\left[n+\frac{1}{2}+\sqrt{y}+\frac{\frac{2\mu V_0}{\hbar^2\alpha}+\frac{2\mu V_{\ell S}r_o^2}{\hbar^2}\left(j(j+1)-\ell(\ell+1)-\frac{3}{4}\right)+\frac{10\mu e^2}{\hbar^2\pi\varepsilon_o\alpha^2R_o^3}}{\left(n+\frac{1}{2}+\sqrt{y}\right)}\right]. \\ \left\{\frac{1}{2\sqrt{y}}\left[\left(-\frac{4V_{\ell S}r_o^2}{\hbar^2}\left(j(j+1)-\ell(\ell+1)-\frac{3}{4}\right)-\frac{6e^2}{\hbar^2\pi\varepsilon_o\alpha^4R_o^3}\right)+1\right]+\right. \\ \left(\frac{\frac{2V_0}{\hbar^2\alpha}+\frac{2V_{\ell S}r_o^2}{\hbar^2}\left(j(j+1)-\ell(\ell+1)-\frac{3}{4}\right)+\frac{10e^2}{\hbar^2\pi\varepsilon_o\alpha^2R_o^3}}{\left(n+\frac{1}{2}+\sqrt{y}\right)}\right) \\ -\frac{1}{2\sqrt{y}}\left(\frac{\frac{2\mu V_0}{\hbar^2\alpha}+\frac{2\mu V_{\ell S}r_o^2}{\hbar^2}\left(j(j+1)-\ell(\ell+1)-\frac{3}{4}\right)+\frac{10\mu e^2}{\hbar^2\pi\varepsilon_o\alpha^2R_o^3}}{\left(n+\frac{1}{2}+\sqrt{y}\right)^2}\right) \\ \left.-\frac{\left(-\frac{4V_{\ell S}r_o^2}{\hbar^2}\left(j(j+1)-\ell(\ell+1)-\frac{3}{4}\right)-\frac{6e^2}{\hbar^2\pi\varepsilon_o\alpha^4R_o^3}\right)}{\left(n+\frac{1}{2}+\sqrt{y}\right)^2}\right\} \end{array}\right] \quad (58)$$

5 Results and discussion

The analytical solution of the Schrodinger wave equation for the superposition of Hulthen potential, spin-orbit interaction and adjusted Coulomb potential is applied to study two nuclides; calcium 41 and scandium 41 isotopes.

Explicitly: ^{41}Ca and ^{41}Sc nuclei are chosen as nuclear systems in this study, being that the best evidence of single particle behavior is easily observed in near doubly magic nuclei. The nucleus of ^{41}Ca has a closed shell for both nucleons with a valence neutron in the $1f_{\frac{7}{2}}$ level. Also, ^{41}Sc has closed shells for protons and neutrons, with a valence proton in the $1f_{\frac{7}{2}}$ level. The ground state properties of ^{41}Ca and ^{41}Sc are determined by the valence nucleon orbiting the closed core according to the theory of nuclear shell model. We obtain the numerical results of the ground state energies of ^{41}Ca and ^{41}Sc from Eq. (39) and Eq. (38) respectively. Table 1 gives a summary of the parameters used for the numerical calculation. The numerical results of these energies of the nuclei under study are as presented in Table 2 and compared to experimental data culled from ref [13]. The calculated energy levels agree to a very great extent with the experimental values. Comparing the ground state energy of ^{41}Ca obtained from this study to the experimental value shows a percentage relative error of 2.02%. The calculated ground state energy of ^{41}Sc obtained from the present work shows a percentage relative error of only 0.95% to that obtained experimentally. The small percentage relative error recorded here attests to the success of the analytical method employed in this work as well as the excellent means of adding the spin orbit interaction to the Hulthen potential plus the Coulomb potential, which serves as the nuclear potential for the nuclei under study. The physical observables such as the expectation values for position (radius), kinetic energy, and the square of momentum are as presented on Table 3. Using the same set of parameters used for calculating the numerical values for the energies of both nuclei under study, Eq. (51) was used to obtain the numerical values for the position (radius) of the nuclei, Eq. (56) was used to obtain the kinetic energies and Eq. (58) was used to obtain the numerical values for the square momentum of both nuclei. Comparing the

calculated expectation value for the radius of the isotopes under study to the experimental values of their radii showed a relative percentage error of 20.8%.The numerical values for kinetic energy and momentum obtained from this work were not compared to experimental values of these quantities owing to the unavailability of experimental data on these quantities for the isotopes under study.

Table 1 – Numerical values of potential parameters for the combined potential

Parameters	^{41}Ca	^{41}Sc
$\boldsymbol{\alpha}$ (fm^{-1})	0.5	0.5
$\boldsymbol{V_o}$ (MeV)	45.83	45.83
$\boldsymbol{V_{LS}}$ (MeV)	20.1652	20.1652
$\boldsymbol{\hbar c}$ (MeV)	197.3269602	197.3269602
$\boldsymbol{\mu}$ (MeV/c^2)	915.20392928	915.212583522
$\boldsymbol{R_o}$ (fm)	4.1378607	4.178607
$\boldsymbol{\varepsilon_0}$	0.079785	0.079785
$\boldsymbol{r_o}$	0.2	0.2
e(MeV)	-	1.199999999

Table 2 – Ground state energy of ^{41}Ca and ^{41}Sc

Nuclides	State	Calculated Energy (MeV) {present work}	Experimental value of Energy (MeV)[23]
$\boldsymbol{^{41}Ca}$	$1f_{\frac{7}{2}}$	-357.51025	-350.4148
$\boldsymbol{41Sc}$	$1f_{\frac{7}{2}}$	-346.41183	-343.1371

Table 3 – Numerical results of the expectation values for radius, kinetic energy and square of momentum of ^{41}Sc and ^{41}Ca isotopes

Quantity		**^{41}Sc**	**^{41}Ca**
Radius $\langle \boldsymbol{r^2} \rangle^{\frac{1}{2}}$ (fm)	Calculated value	2.74591	2.75152
	Experimental value (Angeli et al)	3.4698	3.4780
Kinetic energy $\langle \boldsymbol{T} \rangle$ (eV)	Calculated value	342.86341	337.22125
	Experimental value	-	-
Square of momentum $\langle \boldsymbol{P^2} \rangle$	Calculated value	6.27580 X 10^5	6.17251 X 10^5
	Experimental value	-	-

6 Conclusions

In this study, we obtained the approximate solution of the Schrodinger wave equation for the superposition of Hulthen potential with spin-orbit potential plus adjusted Coulomb potential using the NU method. Clearly, we calculated the single particle energy spectrum for this constructed potential model and applied it to obtain the ground state energy of near doubly magic nuclei, namely, ^{41}Ca and ^{41}Sc. We also obtained the single particle normalized wave function for the nuclei under study. Using the Hellman-Feynman theorem, the physical observables such as the radius, kinetic energy and momentum of selected near doubly magic nuclei were calculated in this study. Therefore, we propose that our constructed potential model can be used to study nuclei such as near doubly magic and near singly magic nuclei.

References

1 A. De-Shalit, I. Talimi, Nuclear shell theory. Weizmann Institute of Science, Rehovoth, Isreal, 1962.

2 M. G. Mayer, J. H. D. Jensen, Elementary theory of nuclear shell structure, Wiley, New York, 1955.

3 B. R. Barrett, D. J. Dean, M. Hjorth-Jensen, J. P. Vary. Nuclear forces and the quantum many-body problem // Journal of physics G. Nuclear and particle physics. – 2005. – Vol. 31. – P. 8. https://doi.org/10.1088/0954-3899/31/8/E01

4 B. L. Cohen, I. B. L. Cohen. Concepts of Nuclear Physics, McGraw-Hill Companies, New York, USA, 1971.

5 M. A. Preston, R. K. Bhaduri. Structure of the nucleus, CRC Press, 2018.

6 H. Heylen. Ground state properties near the N = 20 and N = 40 Islands of inversion. PhD dissertation, MPG Germany, 2016.

7 S. G. Nilson, I Ragnarsson. Shapes and shells in nuclear structure, Cambridge University Press, Cambridge, 100, 1995.

8 S. Bogner, T. T. S. Kuo, L. Coraggio, A. Covello, N. Itaco. Low momentum nucleon –nucleon potential and shell model effective interactions // *Phys.Rev.C.* – 2002. – Vol. 65. – Pp. 1-5. https://doi.org/10.1103/PhysRevC.65.051301

9 A. Nikman, A. A. Rajabi, M. Solaimani. Solution of D – dimensional Schrodinger equation for Woods-Saxon potential with spin-orbit, Coulomb and centrifugal terms through a new hydrid numerical fitting Nikiforov- Uvarov method // J. Theor. Appl. Phys. -2016. -Vol. 10. -No.1. -Pp. 53-59.

10 K. S. Krane. Introductory nuclear physics 3rd ed., Wiley and Sons Inc., New York, 1988.

11 P. Goldhammer. The structure of light nuclei // Review of modern physics. – 1963. – Vol. 35. – No. 1. – P. 40. https://doi/10.1103/ RevModPhys.35.40

12 H. J Mang, H. A. Weidenmuller. Shell-model theory of the nucleus // Annual Rev. Nucl. Sci. – 1968. – Vol. 18. 1. – Pp. 1-26. https:///doi/ abs/10.1146/annurev.ns.18.120168.000245

13 M. Mousavi, M. R. Shojaei. Calculation of energy and charge radius for doubly-magic nuclei of ^{41}Ca and ^{41}Sc with extra nucleon // Chinese journal of physics. -2016. -Pp. 1-6.

14 R. Sever, C. Tezcan, O. Yesiltas, M. Bucurgat. Exact solution of effective mass Schrodinger equation for the Hulthen potential // Int. J. Theor. Phys. – 2008. – Pp. 2243-2248. https://doi/10.1007/s10773-008-9656-7

15 S. M. Ikhdair, R. Sever. Approximate eigenvalue and eigenfunction solutions for the generalized Hulthen potential with any angular momentum // Journal of Mathematical Chemistry. -2007. – Vol. 42. – No.3. – Pp. 461-471. https://doi/10.1007/s10910-006-9115-8

16 J. Hughes, K. J. Le Couteur. Spin-orbit coupling in the nuclear shell model, Department of theoretical Physics, monograph, University of Liverpool, 1950.

17 E. S. William, E.P. Inyang, E. A. Thompson, Arbitrary l – solution of the Schrodinger equation interacting with Hulthen-Hellman potential model // Rev. Mex. Fis. – 2020. – Vol.66. – No.6. – Pp. 730-741. https://doi.org/10.13349/ RevMesFis.66.730

18 C. O. Edet, U. S. Okorie, A. T. Ngiangia, A. N. Ikot. Bound state solution of the Schrodinger equation for the modified Kratzer potential plus screened Coulomb potential // Indian J. Phys. -2020. -Vol. 94. -Pp. 425-433. https://doi.org/10.26850 /1678-4618eqj.v45.1.2020.p65-77

19 M. R. Pahlavani, S. A. Alavi. Solution of Woods-Saxon potential with spin-orbit and centrifugal terms through Nikiforov-Uvarov method // Comm. Thoer. Phys. -2012. -Vol. 58. -No.5. -Pp. 739-743. http://dx.doi.org/10.1088/0253-6102/58/5/19

20 A. F. Nikiforov, V.B. Uvarov. Special function of mathematical physics, Birkhauser, Basel, 1988.

21 R. L. Greene, C. Aldrich. Variational wave function for screened Coulomb potential // Rev. A. -1976. – Vol. 14. – No. 6. – P. 2363. https://doi.org/10.1103/physRev.14.2363

22 S. H. Dong, W. C. Qiang, G. H. Sun, V. R. Bezerra. Analytical approximation to the l-wave solution of the Schrodinger equation with the Eckart potential // J. phys. A.: Mathematical & Theoretical. -2007. – Vol. 40. – No.34. – Pp. 1-7.

23 C. A. Ebomwonyi, M. C. Onate, M. C. Onyeaju, A. N. Ikot. Any l state solution of the Schrodinger equation interacting with Hellmann generalized Morse potential model // Karbala Intl. J. Mod. Sc. – 2017. – Vol. 3. – No.1. – Pp. 1-10. http://dx.doi.org/10.1016/j.kijoms.2017.03.001

24 A. Tas, O. Aydogdu, M. Salti. Relativistic spinless particle with position dependent mass: Bound state and scattering phase shift // J. Korean Phys. Soci. -2017. – Vol.70. – No.10. – Pp. 896-904. https://doi:10.1007/s12648-020-01908-y

25 D. Wallace. An introduction to Hellmann-Feynman theory, M. Sc. Thesis, Department of Mathematics, University of Central Florida, Orlando, USA, 2005.

26 I. Angeli, K. P. Marinova, Table of experimental nuclear state charge radii: An update, atomic data and nuclear data table. – 2013. – Vol. 99. – No. 1. – Pp. 69-95. https://doi.10.1016/j.adt.2011.12.006

IRSTI 29.19.22 https://doi.org/10.26577/phst.2021.v8.i2.03

Optical properties of dextran-stabilized silicon nanoparticles in aqueous medium

A. Yu. Kharin[1] and V. Yu. Timoshenko [1,2*]

[1] National Research Nuclear University "MEPhI", Phys-Bio Institute, Moscow, Russia
[2] Lomonosov Moscow State University, Faculty of Physics, Moscow, Russia
*e-mail: timoshen@physics.msu.ru

Silicon nanoparticles (Si-NPs) with initial sizes of the order of 100 nm were prepared by femtosecond laser ablation-fragmentation of microcrystalline silicon in water followed by drying and resuspending in water or in aqueous solutions of dextran. The prepared aqueous suspensions of Si-NPs without dextran and with dextran coating were investigated by means of the scanning electron microscopy, dynamic light scattering and optical absorption spectroscopy in the spectral range from 250 to 800 nm. The optical absorption of uncoated Si-NPs in an aqueous medium with different pH-level varied from 4 to 8 was found to decrease with time because of a process of the dissolution of those NPs in water. The dissolution rate depended nonmonotonically on the solution acidity (pH level) and the corresponding times were in the range from 50 to 180 hours. The addition of dextran into the solution was found to significantly decrease the dissolution rate of Si-NPs to 300 hours because of the coating of NPs with a polymer shell. The obtained results can be useful to develop new biomedical technologies involving Si-NPs as stabilized theranostics (therapy and diagnostics) agents.

Key words: nanoparticles, dextran, biopolymer, optics, absorbance.
PACS number: 61.82.Pv.

1 Introduction

Since the first observation of the room temperature photoluminescence of porous silicon (PSi) [1], publications involving the use of silicon nanoparticles (NPs) for biomedical purposes have become increasingly frequent. Silicon (Si) NPs can be used for diagnostics as optical markers [2], nonlinear optical tags [3], contrast agents for magnetic resonance imaging (MRI) [4], and for the treatment of oncological diseases [5], as well as carriers of drugs [6,7]. The rapid degradation of PSi-NPs in water with the formation of silicate anions ensures the removal of injected NPs from the body. Too rapid dissolution of PSi-NPs can be prevented by modifying the surface of PSi-NPs, for example, by biopolymer coating with PVA-PLGA molecules [8-10].

Despite the low cytotoxicity of Si-NPs themselves [11] and their relatively rapid degradation in aqueous media [12], biomedical applications of PSi-NPs are limited due to the high toxicity of the porous silicon precursor – hydrofluoric acid (HF), so the more clean and mild synthesis approaches such as laser ablation or laser fragmentation of target in liquid [13] or plasmochemical [14] method attract more attention [15]. These kinds of Si-NPs have low toxicity [16,17], but there is no accurate description of the dissolution kinetics for Si-NPs produced by the laser ablation-fragmentation method.

In this research, we have studied the optical properties of Si-NPs in aqueous media with different pH. In addition, the sorption of dextran molecules in an aqueous solution onto the surface of Si-NPs was investigated, and the optical properties and kinetics of dissolution of the polymer-coated Si-NPs were studied in the solutions with different pH-level.

2 Materials and methods

In this work, we used Si-NP, which were obtained by laser fragmentation of microcrystalline silicon dispersed in deionized water [18]. The fragmentation was carried out for 1 hour using a Ti-sapphire laser with a wavelength of 800 nm. The pulse duration was 130 fs, and the pulse energy was 300 mJ. The pulse frequency was 1 kHz. Laser irradiation was focused by a lens into the center of the cuvette.

During fragmentation, the solution was stirred using a magnetic stirrer. Further, the resulting NPs were dried and dispersed in water to obtain a stock solution with a concentration of 50 mg/mL. Then 10 mg of dextran (molar mass 35-45 kDa) were added to 2 mL of the stock solution of Si-NPs and sonicated using an ultrasonic bath for 15 min.

Dissolution kinetics for diluted Si-NPs solutions with different pH, which was adjusted by adding drops of HCl and KOH solutions, were investigated by means of the optical extinction spectroscopy using a Cary 60 UV–Vis spectrometer in the spectral region of 250-800 nm. For this, samples of mother liquors were diluted in distilled water until a concentration of 0.1 mg/mL was reached, and then the extinction spectra were measured for different storage time of the suspension.

The colloidal stability of Si-NPs in aqueous media was analyzed by using a method of the dynamic light scattering (DLS) with a Zetasizer Nano ZS DLS analyzer (Malvern, UK), which was also used for measurements of the electrokinetic zetta-potential (ZP) of Si-NPs. The DLS data were processed using the Zetasizer Software. The structural properties and composition of the dried NPs were investigated by means of the scanning electron microscopy (SEM) with a Tescan MAIA 3 (Tescan, Czech Republic) SEM.

3 Results and discussion

Measurements of DLS and ZP confirm the presence of dextran on the surface of Si-NPs dispersed in the dextran solution. Figure 1a shows size distribution where the black curve and red one corresponds to the initial Si-NPs and dextran-coated ones, respectively. The hydrodynamic size of Si-NPs in diluted stock solution is 100 ± 30 nm, while the average particle size of dextran-exposed Si-NPs is 275 ± 50 nm, which may indicate that Si-NPs are covered with a polymer layer. The increase of the hydrodynamic size of Si-NPs in the dextran solution in comparison with that for initial Si-NPs can be also related to agglomeration of the former NPs.

Figure 1b and Figure1c show SEM images of the initial and dextran-coated Si-NPs, respectively. Besides the larger sizes of individual NPs, the Si-NP aggregates with sizes above 250-300 nm are also present in the latter sample. Therefore, the SEM data confirm the increase of the NP size in the dextran solution, than can be related the de dextran-coating of those NPs.

The NP's surface charge state is defined by the pH level of media and acidity of the surface groups. Therefore, the electrokinetic zeta-potential of surface-coated NPs can be different from the initial one. Figure 2 shows dependences of the zeta-potential of initial and dextran-coated Si-NPs in aqueous solutions versus the pH-level.

The sharp drop in the pH-dependence of ZP for Si-NPs in dextran solution and its more smooth behavior in the case of initial Si-NPs can be explained by different parameters of the surface groups, which are modified in the presence of dextran molecules. Taken together, these observations provide strong evidences that the surfaces of Si-NPs are actually coated with dextran molecules in aqueous solution.

Figure 3 shows extinction spectra of Si-NPs dispersed in water and in dextran solution. Since in this spectral region Si-NPs are characterized by a large absorption cross-section the extinction value can be approximately equal to the absorption. Both spectra exhibit a maximum in the UV region (see Fig. 3), which is associated with the direct band gap absorbance in crystalline Si. While the spectrum for initial Si-NPs exhibits a shoulder in the region of 400-600 nm, which can be attributed to the Mie scattering from individual Si-NPs with sizes about 100 nm [3], the absorption spectrum of dextran-coated Si-NPs shows more smooth decrease of the absorption in the investigated spectral region. This fact can be related to the larger sizes of dextran-coated Si-NPs.

To study the kinetics of dissolution of Si-NPs in aqueous medium, the integral absorption intensity in the range of 400-600 nm is calculated and analyzed. Figure 4a and Figure 4b show dependences of the spectrally integrated absorption of Si-NPs in aqueous suspension with different pH-level on time for initial Si-NPs and dextran-coated ones, respectively.

At low concentrations of Si-NPs, the absorption is proportional to the concentration of NPs in the colloid. The absorption intensity (Fig. 4) decreases with time of the storage Si-NPs in aqueous media.

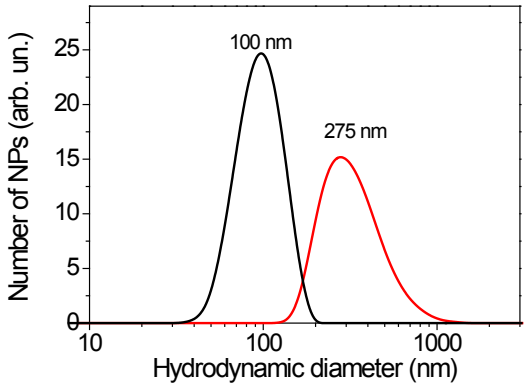

a

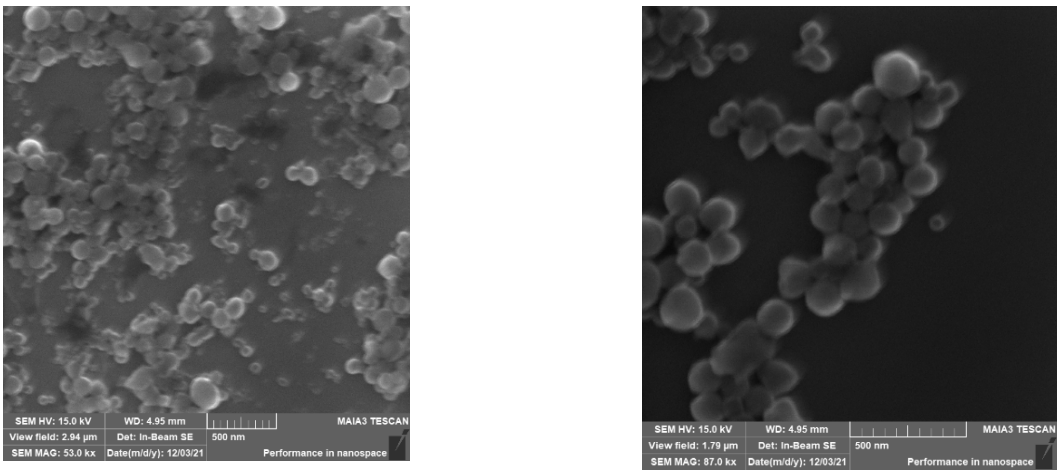

b c

Figure 1 – (a) Size distribution of Si-NPs in aqueous suspensions without dextran (black curve) and with dextran (red curve). The sizes were estimated immediately after the synthesis of colloids; (b) and (c) SEM images of Si-NPs before and after coating with dextran, respectively

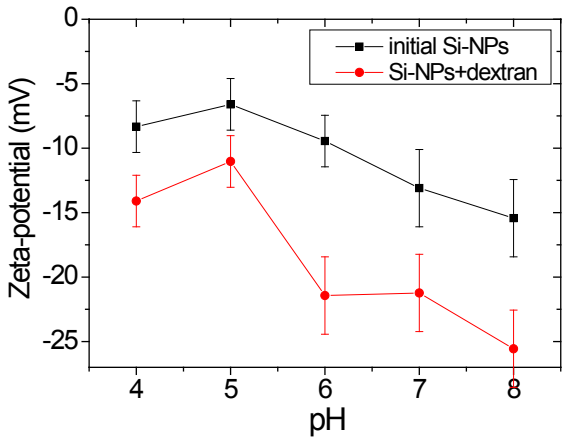

Figure 2 - Dependences of the zeta-potential of initial and dextran-coated Si-NPs versus pH-level of the aqueous solution

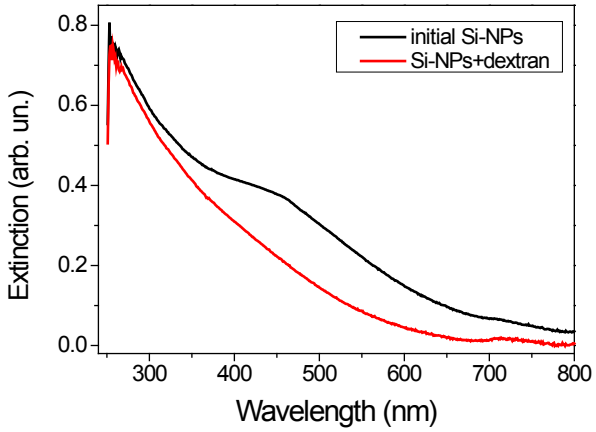

Figure 3 – Extinction spectra of aqueous suspensions of initial and dextran-coated Si-NPs

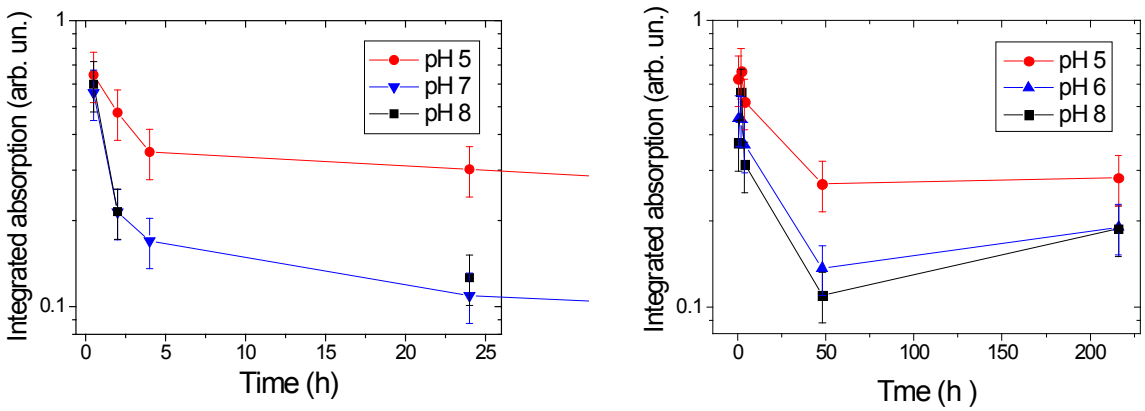

Figure 4 – Dependences of the spectrally integrated absorption of Si-NPs in aqueous suspension with different pH-level on time for (a) initial S-NPs and (b) dextran-coated Si-NPs

If we assume that the dissolution of Si-NPs is a first-order process, the dissolution rate is proportional to the number of NPs, then it is possible to describe the time dependence of the NPs' concentration can be expressed as follows:

$$C(t)=C_0e^{-kt}, \quad (1)$$

where C_0 is the initial NPs' concentration, is the characteristic dissolution rate, , and is the dissolution time.

The general view of the dependences confirms the assumption that the concentration of Si-NPs decreases exponentially with time. The approximation of the curves in Fig. 5 allows one to obtain the characteristic times of nanoparticles dissolution. The dependence of these times on pH is shown in Fig. 5. It is important to note that at pH=7, no decrease in the absorption was observed for the coated nanoparticles. For this reason, this point is not plotted in the graph. It is worth noting that half of the Si-NPs coated with dextran are stable in a solution with any pH level for at least 300 hours (see Fig.4b). This fact indicates a high level of the surface stabilization of Si-NPs by dextran molecules.

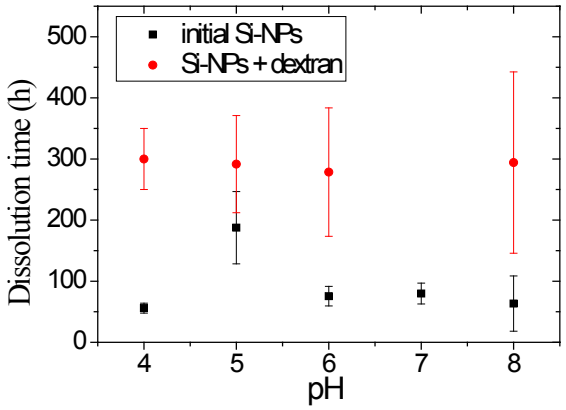

Figure 5 – Dependences of the characteristic degradation times of nanoparticles on pH for dextran-coated (red) and initial (black) Si-NPs

It is seen that uncoated Si-NPs are well dissolvable both into the strongly acidic and alkaline solutions, and at pH=5 the dissolution rate is noticeably slower. The dissolution rate of dextran-doated Si-NPs does not depend on pH and is significantly lower than one for the initial Si-NPs.

4 Conclusions

The kinetics of dissolution of uncoated Si-NPs in aqueous media are strongly dependent on the pH level of the solution. The addition of dextran into the solution can significantly slow down the dissolution of Si-NPs that is associated with the coating of those NPs with the polymer shell. Since the investigated dextran is approved for clinical use, the results obtained can stimulate the development of new biomedical technologies using silicon nanoparticles.

Acknowledgments

Authors acknowledge A.V. Kabashin for providing samples of nanoparticles and stimulating discussions, as well E. Semenchuk for the assistance with absorbance data collection. A.Yu.K. acknowledges the support by the Grant of the President of the Russian Federation – for state support of young Russian scientists – MK-5375.2021.1.3. V.Yu.T. thanks the support by the Grant from the Ministry of Science and Higher Education of the Russian Federation (FSWU-2020-0035).

References

1 L.T. Canham. Silicon quantum wire array fabrication by electrochemical and chemical dissolution of wafers // Appl. Phys. Lett. –1990. – Vol.57. – Pp.1046-1048. https://doi.org/10.1063/1.103561

2 Z.F. Li, E. Ruckenstein. Water-soluble poly (acrylic acid) grafted luminescent silicon nanoparticles and their use as fluorescent biological staining labels // Nano Letters. – 2004. – Vol.4. – Pp.1463-1467. https://doi.org/10.1021/nl0492436

3 A.Yu. Kharin, V.V. Lysenko, A. Rogov, Yu.V. Ryabchikov, A. Geloen, I. Tishchenko, O. Marty, P.G. Sennikov, R.A. Kornev, I.N Zavestovskaya, A.V. Kabashin, V.Yu Timoshenko. Bi-Modal Nonlinear Optical Contrast from Si Nanoparticles for Cancer Theranostics // Adv. Opt. Mat. – 2019. –Vol.7. – Pp.1801728. https://doi.org/10.1002/adom.201801728

4 V. M. Fomin, V.Yu. Timoshenko. Spin-Dependent Phenomena in Semiconductor Micro-and Nanoparticles—From Fundamentals to Applications // Appl. Sci. – 2020. – Vol.10. – Pp.4992. https://doi.org/10.3390/app10144992

5 V.A. Oleshchenko, A. Yu. Kharin, A.F. Alykova, O.V. Karpukhina, N.V. Karpov, A.A. Popov, V.V. Bezotosnyi, S.M. Klimentov, I.N. Zavestovskaya, A.V. Kabashin, V. Yu. Timoshenko. Localized infrared radiation-induced hyperthermia sensitized by laser ablated silicon nanoparticles for phototherapy applications // Appl. Surf. Sci. – 2020. – Vol.516. – Pp.145661. https://doi.org/10.1016/j.apsusc.2020.145661

6 E.J. Anglin, L. Cheng, W.R. Freeman, M. J. Sailor. Porous silicon in drug delivery devices and materials // Adv. Drug Del. Rev. – 2008. – Vol.60. – Pp.1266-1277. https://doi.org/10.1016/j.addr.2008.03.017

7 M.A. Konoplyannikov, A.S. Eremina, Yu.V. Kargina, I.M. Le-Deygen, A.Yu. Kharin, T. Yu. Bazylenko, G.M. Yusubalieva, V.A. Revkova, O.N. Matchuk, I.A. Zamulaeva, M. R. Abramova, S.L. Kotova, P.S. Timashev, V.P. Baklaushev, V.Yu. Timoshenko. Mesoporous silicon nanoparticles loaded with salinomycin for cancer therapy applications // Micropor. Mesopor. Mat. -2021. –Vol.328. –Pp.111473. https://doi.org/10.1016/j.micromeso.2021.111473

8 J.H. Park, L. Gu, G. v. Maltzahn, E. Ruoslahti, S.N. Bhatia, M.J. Sailor. Biodegradable luminescent porous silicon nanoparticles for in vivo applications // Nat. Mat. –2009. –Vol.8. –Pp.331-336. https://doi.org/10.1038/nmat2398

9 M.B. Gongalsky, A.Yu. Kharin, L.A. Osminkina, V. Yu. Timoshenko, J. Jeong, H. Lee, B.H. Chung. Enhanced photoluminescence of porous silicon nanoparticles coated by bioresorbable polymers // Nanosc. Res. Lett. –2012. –Vol.7. –Pp.1-7. https://doi.org/10.1186/1556-276X-7-446

10 A.S. Eremina, A.Yu. Kharin, Yu.V. Kargina, V.Yu. Timoshenko. Stabilization of porous silicon nanoparticles by PEGalization in water // J. Phys. Conf. Ser. –2021.–Vol.2058. –Pp.012013. https://doi.org/10.1088/1742-6596/2058/1/012013

11 H.A. Santos. Porous silicon for biomedical applications, Woodhead Publ. (2014).

12 M.A. Tischler, R.T. Collins, J.H. Stathis, J.C. Tsang. Luminescence degradation in porous silicon // Appl. Phys. Lett. –1992. –Vol.60. –Pp.639-641. https://doi.org/10.1063/1.106578

13 D. Rioux, M. Laferrière, A. Douplik, D. Shah, L. Lilge, A.V. Kabashin, M.M. Meunier. Silicon nanoparticles produced by femtosecond laser ablation in water as novel contamination-free photosensitizers // J. Biomed. Opt. –2009. –Vol.14. –Pp.021010. https://doi.org/10.1117/1.3086608

14 A.M. Funde, N.A. Bakr, D.K. Kamble, R.R. Hawaldar, D.P. Amalnerkar, S.R. Jadkar. Influence of hydrogen dilution on structural, electrical and optical properties of hydrogenated nanocrystalline silicon (nc-Si: H) thin films prepared by plasma enhanced chemical vapour deposition (PE-CVD) // Sol. Energ. Mat. Sol. Cells. –2008. –Vol.92. –Pp.1217-1223. https://doi.org/10.1016/j.solmat.2008.04.012

15 A. V. Kabashin, V. Yu. Timoshenko. What theranostic applications could ultrapure laser-synthesized Si nanoparticles have in cancer? // Nanomedicine. – 2016. –Vol.11. –Pp.2247-2250. https://doi.org/10.2217/nnm-2016-0228

16 N. O. Farrell, A. Houlton, B.R. Horrocks. Silicon nanoparticles: applications in cell biology and medicine // Int. J. Nanomedicine. –2006. – Vol.1. –Pp. 451–472. https://doi.org/10.2147/nano.2006.1.4.451

17 N.V. Sharonova, E.V. Svirshchevskaya, A.A. Popov, N.V. Karpov, G.V. Tikhonovskiy, A.Yu. Zakharkiv, S.V. Sizova, V.Yu. Timoshenko, S.M. Klimentov, V.A. Oleinikov. Interaction of SiFe Nanoparticles with Epithelial and Lymphoid Cells // Russ. J. Bioorg. Chem. – 2020. –Vol.46 – Pp.1198-1206. https://doi.org/10.1134/S106816202006028X

18 P. Blandin, K. A. Maximova, M. B. Gongalsky, J. F. Sanchez-Royo, V. S. Chirvony, M. Sentis, V.Yu. Timoshenko, A.V. Kabashin, Femtosecond laser fragmentation from water-dispersed microcolloids: toward fast controllable growth of ultrapure Si-based nanomaterials for biological applications // J. Mater. Chem. B. – 2013. –Vol.1. –Pp. 2489-2495. https://doi.org/10.1039/C3TB20285B

IRSTI 28.17.23 https://doi.org/10.26577/phst.2021.v8.i2.04

Simulation of non-isothermal liquid sprays under large-scale turbulence

A. Askarova[1], S. Bolegenova[1], Sh. Ospanova[1*], N. Slavinskaya[2], A. Aldiyarova[1] and N. Ungarova[1]

[1]Physics and Technology Department, Al-Farabi Kazakh National University, Almaty, Kazakhstan
[2] Institute of Combustion Technology, German Aerospace Centre (DLR), Stuttgart, Germany
[*]e-mail: Shynar.Ospanova@kaznu.kz

Due to the high level of achieved research, there are prospects for the widespread use of the method and specific physical results in the areas under consideration, as well as ways for more effective application of mathematical modeling methods using modern computing technology in various subject areas. For the numerical study of the combustion of liquid fuels, it is required to consider many complex interrelated processes and phenomena, which are laborious tasks of computational thermal physics. In the theory's study of combustion and the development of various technical devices, the actions of which are based on the use of the combustion process, a computational experiment is becoming an increasingly important element. Computational fluid dynamics methods have become widespread in technical physics when it becomes possible to optimize an experiment based on its virtual prototype. This work is devoted to the numerical modeling of the processes of breakup, dispersion, evaporation and combustion of liquid fuel droplets under high turbulence. Fundamental characteristics, methods of liquid fuels atomization, the mathematical model and basic equations describing the collision, distribution and combustion of liquid fuels at high turbulence are presented. Results of computational experiments by determination of the optimal conditions for the combustion of liquid hydrocarbon fuel are presented. Influence of the oxidant's initial temperature on the processes of atomization and dispersion of droplets in the combustion chamber under high turbulence is investigated. Optimal combustion parameters for the dodecane have been determined.

Key words: numerical modeling, atomization, liquid fuel, dodecane, high turbulence.
PACS number: 07.05.Tp.

1 Introduction

One of the main global problems of the urbanized countries including Kazakhstan, is the emission of pollutants into the atmosphere. Almaty is the city of Kazakhstan with the greatest traffic congestion. The Statistics Department of Almaty fixes the increased concentration of harmful substances (small suspended particles) in the air on a weekly basis. Small suspended particles PM2.5 and PM10 are in the atmosphere as an aerosol; because of their low weight, they can't settle to the ground. The World Health Organization PM10 and PM2.5 are classified as priority pollutants. PM2.5 particles are actually soot, dust, micro-fragments of asphalt and rubber, mineral salts (sulfates, nitrates) and heavy metal compounds (mainly oxides). They are got because of the work of some industries, but often an increase in their concentration is provoked by cars, namely the combustion of liquid fuel [1-6].

The course of chemical reactions under conditions of dynamic and thermal interaction of reagents, phase transformations accompanying intensive mass transfer of reagents, the influence of the thermodynamic state of the system and its structural characteristics on the process parameters are the distinctive features of the combustion of liquid fuels. The problem of fundamental research of the regularities of heat and mass transfer processes during the combustion of various types of liquid fuel requires a detailed study of the theory of combustion.

A lot of problems arising in thermal physics and technical physics associate with the numerical solution of the Navier-Stokes equations systems, which is the basis of continuum mechanics.

Therefore, in connection with the ever-increasing use of numerical research in solving scientific and technical problems, it is important to ensure the greatest possible scientific and practical side of the issue. It can only achieve this through careful application of numerical modeling methods in various subject areas. [7, 8].

The efficiency of fuel use, and, ultimately, the productivity and environmental friendliness of the installation, depends on the correct (optimal) organization of fuel combustion, including the processes of fuel preparation, fuel supply and rational combustion. All research on creating efficient internal combustion engines is aimed at reducing the amount of pollutants emitted by vehicles into the atmosphere. Emissions from gasoline and diesel internal combustion engines contain carbon dioxide (CO_2) and carbon monoxide (CO). Partially combusted fuels are also present in the exhaust gases, which form a complex mixture of hydrocarbons (HCs) such as methane (CH_4). Also, in the composition of combustion products, solid particles and nitrogen oxides (NO_x) are emitted, the latter are a common component of diesel emissions [9, 10].

Organization of high-quality combustion of fuel largely influences the problems of saving energy resources and improving the ecological state of heat engines. However, the technologies for the preparation and combustion of fuel are practically brought to perfection, and the efficiency and environmental cleanliness of internal combustion engines in most cases leaves much to be desired. The problem arises from searching for new methods in this area. Modeling of breakup, dispersion, evaporation and combustion processes of liquid fuel droplets under various initial conditions applies to solving the posed problems.

Since 2019, any vehicle for public roads imported into the Republic of Kazakhstan permanently and from the countries of the Customs Union must comply with the Euro-5 standard. Using fuel inappropriate for the ecological class by vehicles leads to premature wear of vehicle exhaust systems and unjustified costs for consumers of equipment. Engines with a fuel analyzer under the Euro 5 standard create difficulties in operation outside of large cities where low quality fuels are used. Here, it automatically reduced the engine speed until it stops completely. Besides the obvious positive environmental effect, the entry into force of stricter regulations will stimulate the production of more modern types of vehicles and introducing technologies in engine building. In addition, there is an opportunity to create new industries in the automotive industry, primarily in the production of components and components.

Also, since January 1, 2018, Kazakhstan has completely switched to the use of motor fuel of environmental standards not lower than Euro-4 and Euro-5. Now gasoline and diesel fuel supplied at retail must comply with the K4 and K5 environmental classes. Using these fuels will reduce emissions of harmful substances [11, 12].

In connection with the above, intensification of production, decrease in the material consumption of equipment, an economical consumption of fuel and environmental protection are gaining special significance and relevance. It is very important to create a scientific basis for intensive technological processes that ensure the integrated use of fuel and its waste, excluding the harmful effects of production on the biosphere. The new strategy for nature protection and energy conservation involves the selection of the most effective achievements of scientific and technological progress. Three major groups of measures stand out among them: utilization, energy modernization and intensive energy saving.

On July 1, 2021, a new Environmental Code will come into force in Kazakhstan, which complies with international legislative standards in environmental protection. Kazakhstan has become the first country in the post-Soviet space where the idea of a “green economy” is being implemented. On May 30, 2013, Government approved the Concept for the Transition of the Republic of Kazakhstan to a Green Economy.

For a comprehensive experimental study of two-phase flows, it becomes necessary to use special equipment and special working bodies (it is necessary to form a flow of drops of a certain size and a component composition), as well as to develop and use special methods for measuring flow parameters and corresponding measuring equipment, which complicates this process. The development of mathematical modeling of these types flows and the modern power of electronic computers make it possible to a certain extent to get data on the behavior of a two-phase flow, but without obtaining experimental data that allow checking the mathematical models used, it is impossible to verify the adequacy of their application and the accuracy of the results. In the light of such difficulties, phenomenological models of such flows are increasingly being applied.

The engines of the current generation of cars differ significantly from those that were used several decades ago. The main combustion process in engines remains the same, but the injections differ significantly.

Modern internal combustion engines use high-tech fuel injectors to deliver fuel to the engine in the most efficient way. There are different fuel injection systems depending on the type of engine. The most commonly used engines are spark ignition (SI), port injection (PFI or GDI) and direct injection (DI) engines. In spark ignition engines, the injection pressure ranges from 2 to 3 bar and in direct injection engines from 100 to 200 bar. Diesel engines with direct injection operate at much higher pressures. These values are about 10 times or more than spark ignition engines. Injection systems are usually electronically controlled, since the opening and closing of the injector must be quick, which reduces fuel waste [13].

Liquid and gaseous fuels are burned only in a flare, and the liquid fuel is pre-sprayed into small droplets. The characteristics of the combustion process are influenced by several factors: the furnace design, the oxygen concentration of the supplied air for combustion, the pressure at which combustion occurs, etc. Combustion of liquid fuel is a multi-stage process.

Liquid fuel in the first stage is heated to boiling point and evaporates, and in the second stage, combustion occurs. The combustion scheme of a drop in liquid fuel is shown in Figure 1. Because the boiling point of liquid fuel is lower than the ignition temperature, its droplets first evaporate, and then the process of fuel combustion occurs. Because of diffusion through the resulting combustion products, air penetrates to the combustion surface. The combustion rate depends on the size of the burning surface, and the size of the burning surface depends on liquid fuel atomization: the finer the atomization, the greater the rate and completeness of combustion.

A combustion zone is established near the drop on a spherical surface, the diameter of which is 1–5 times larger than the drop size. The droplet evaporates because of the heat of radiation from the combustion zone. In the space between the droplet and the combustion zone, there are liquid fuel vapors and combustion products, in the space outside the combustion zone – air and combustion products. Fuel vapor diffuses into the combustion zone from the inside, and oxygen from outside. Here, these components enter a chemical reaction, which is accompanied by the release of heat and the formation of combustion products.

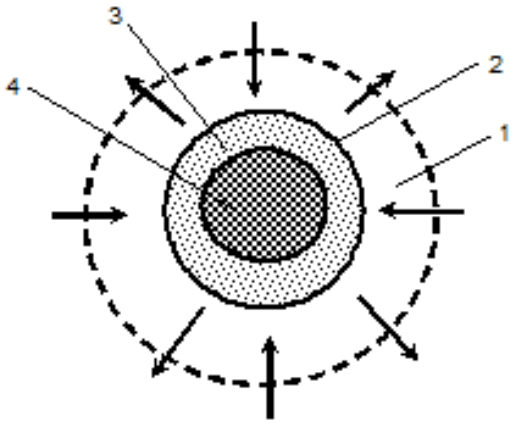

1 – area of diffusion of oxidizer and combustion products, 2 – liquid, 3 – fuel vapor, 4 – liquid fuel drop

Figure 1 – Scheme of the individual liquid fuel drops combustion

2 Mathematical model of the problem

In many experimental studies, it was found that many dimensionless scale parameters are involved in the primary sputtering process [14-16]. Among these parameters are the Weber and Reynolds numbers:

$$We = \frac{\rho_g \left(u_{g,0} - u_{l,0}\right)^2 D_l}{2\sigma}, \qquad (1)$$

$$\mathrm{Re}_l = \frac{u_{l,0} D_l}{\nu_l}, \ \mathrm{Re}_g = \frac{u_{g,0}\left(D_g - D_l\right)}{\nu_g}, \qquad (2)$$

$u_{l,0}$ is the inlet velocity of the liquid, $u_{g,0}$ is the inlet velocity of the gas flow, σ is the coefficient of surface tension, D_l is liquid jet inlet diameter, D_g is the inlet size of the concurrent gas jet. The main parameters also include the ratio of densities, mass and dynamic pressure of the gas and liquid phase: ρ_l / ρ_g, $m = \frac{\rho_g u_{g,0}\left(D_g^2 - D_l^2\right)}{\rho_l u_{l,0} D_l^2}$ and $M = \frac{\rho_g u_{g,0}^2}{\rho_l u_{l,0}^2}$. Of these three parameters, the last one is of primary importance, namely the ratio of impulses:

$$M = \frac{\rho_g u_{g,0}^2}{\rho_l u_{l,0}^2}. \quad (3)$$

Inside the coaxial nozzle moving at a high speed gas flow forms a boundary layer at a rigid interface between two parallel gas and liquid flows. Dimensionless thickness of the incoming boundary layer is also a very important parameter:

$$\frac{\delta_g}{D_g - D_l}. \quad (4)$$

We can also note the Onezorge number as another important parameter:

$$Oh = \frac{\mu_l}{\sqrt{\rho_l \sigma D_l}}. \quad (5)$$

At the exit the boundary layer interacts with the liquid jet and leads to the Kelvin-Helmholtz instability on the free surface. According to the [17], the thickness of the incoming boundary layer controls the most unstable longitudinal wavelength of the Kelvin-Helmholtz instability δ_g. At high Weber numbers, according to the [18], the instability wavelength λ_{KH} is:

$$\lambda_{KH} \approx C_{KH} \sqrt{\frac{\rho_l}{\rho_g}} \delta_g. \quad (6)$$

Here, for coaxial sputtering by an air flow $C_{KH} = 2$, which corresponds to the measurements of the [17]. It can be used the Blasius transformations for the boundary layer thickness $\delta_g = C_\delta \frac{D_g - D_l}{2\sqrt{\mathrm{Re}_g}}$ and the Reynolds number $\mathrm{Re}_g = \frac{u_{g,0}\left(D_g - D_l\right)}{\nu_g}$ [19]. From, measurements of the [18] it was found that $C_\delta = 5.6$.

The development of the Kelvin-Helmholtz instability is called the primary phase of instability. The outflowing jet depends on the large-scale instability of the flow. Then the waves of the primary instability are exposed to the gas flow then they are sped up. This leads to the rapid development of the Rayleigh–Taylor instability in the transverse direction [20, 21]. The onset of this type of instability is called the secondary phase of instability. The expression for very long wavelengths with the Rayleigh-Taylor instability can be written as follows [21]:

$$\lambda_{RT} = 2\pi \sqrt{\frac{3\sigma}{\rho_l a}}, \quad (7)$$

where α means the free acceleration of the fluid. A rapidly moving gas, which produces primary droplets of size separate and fragment filaments of order:

$$r \sim \frac{1}{2} \lambda_{RT}. \quad (8)$$

These droplets can be subjected to a secondary atomization process, forming an injection. It can be noted that discovered an important effect of the liquid injection rate on the droplet size. As for the typical droplet size in the far injection field, it is usually determined by the critical or maximum stable size when the destructive hydrodynamic forces are balanced by capillary forces:

$$r_{cr} = We_{cr} \sigma / \rho_g u_{rel}^2, \quad (9)$$

where u_{rel} is the relative velocity between liquid and gas, We_{cr} is the critical Weber number, the value of which equals 6 large intervals of the Onezorge numbers [17].

The question is how to evaluate u_{rel}. Kolmogorov in his work assumes that a drop in a turbulent flow is stretched until the moment when this extension is of the order of the surface tension force [18]. It then evaluates the value u_{rel} from the expression for the typical increment of gas velocity in a uniform, steady-state turbulent flow. If ε is the dissipation rate, then:

$$r_{cr} = \frac{1}{2} \left(\frac{We_{cr} \sigma}{\varepsilon^{2/3} \rho_g} \right)^{3/5}. \quad (10)$$

These expressions do not consider the density of the liquid. A drop that moves in a turbulent flow will respond to its turbulent expansion only partially because of its inertia. The authors of works used the following expression [20, 22]:

$$\left\langle u_{rel}^{\ 2} \right\rangle \approx \varepsilon \tau_{st}, \qquad (11)$$

where τ_{st} is the Stokes time:

$$\tau_{St} = \frac{2\rho_l r^2}{9\rho_g \nu_g} \frac{1}{1+0{,}15\,\mathrm{Re}_p^{\,0{,}687}}. \qquad (12)$$

Using this expression, one can assume:

$$r_{cr} = \frac{1}{2}\left(\frac{We_{cr} 18 \nu_g \sigma}{\varepsilon \rho_l}\right)^{1/3}. \qquad (13)$$

Both relations are valid when the post-spray mechanism is related to turbulence in the gas flow.

3 Physical statement of the problem

A model of a combustion chamber as a cylinder, the height of which is 15 cm, diameter is 4 cm have been used. The general view of the combustion chamber is shown in Figure 2. The computational domain comprises 650 cells. Liquid fuel is injected by a nozzle in the center of the lower part of the combustion chamber. Temperature of the combustion chambers walls was 353 K. The initial temperature of the gas in the combustion chamber was 700 K, the fuel was injected at 300 K. The initial radius of the injected droplets was 25 microns. Angle at which the droplets are injected was 10^0. Pressure in the combustion chamber was 80 bar, the injection speed of the liquid fuel was 250 m/s.

In this work the simulation results of the processes of atomization, dispersion and combustion of liquid fuels in a cylindrical combustion chamber are presented. In this work, the liquid fuel dodecane is used. The chemical reaction of this fuel combustion in the chamber is presented below. This reaction leads to the formation of carbon dioxide and water:

$$2C_{12}H_{26} + 37O_2 \rightarrow 24CO_2 + 26H_2O\,.$$

The results of a numerical simulation of the dodecane combustion depending on the initial temperature of the oxidizer in the combustion chamber are presented. In the [23-27] works, similar studies were got by using numerical modeling at high turbulence, where the optimal values of pressure and mass for dodecane were determined. Thus, for dodecane at the initial moment of time, the values of pressure and mass were 80 bar and 7 mg. In this work, all calculations were got at optimal values of pressure and mass, which were taken from the works of the above authors, and the initial temperature in the combustion chamber varied from 700 K to 1500 K.

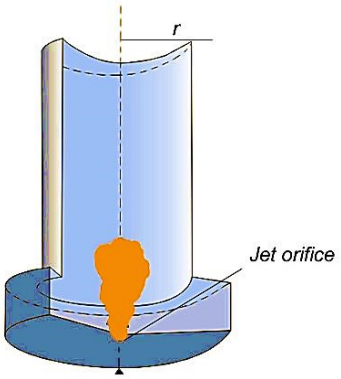

Figure 2 – General view of the combustion chamber

4 Numerical simulation results

Analysis of Figure 3 shows that if the temperature of the oxidizer in the combustion chamber takes values above 800 K, then the fuel burns more intensively, a large amount of heat is released and the combustion chamber heats up to 3000 K. In this case, the initial temperature of the oxidizer has the greatest effect on the combustion of dodecane since an increase in the initial temperature from 900 K to 1500 K leads to an increase in the maximum temperature from 2080.09 K to 2684.69 K.

Figure 4 shows the distribution of the maximum concentration of carbon dioxide for dodecane depending on the initial temperature of the oxidizer in the combustion chamber. During the combustion of dodecane, the concentration of the formed carbon dioxide takes on large values. As seen from the figure, with an increase in temperature from 900 K to 1500 K, the concentration of carbon dioxide released during the combustion of dodecane takes values from 0.11986 g/g to 0.14142 g/g.

From the analysis of the curves in Figures 3 and 4, it can be concluded that for dodecane, the optimal initial temperature of the oxidizer in the combustion chamber is 900 K. At this temperature, the fuel quickly reacts with the oxidizer, the chamber heats to high temperatures, and the concentration of the resulting carbon dioxide does not exceed the permissible limits.

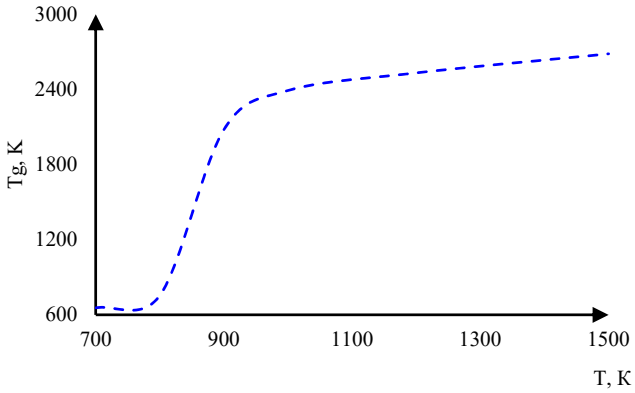

Figure 3 – Dependence of the maximum combustion temperature on the initial temperature of the oxidizer in the combustion chamber

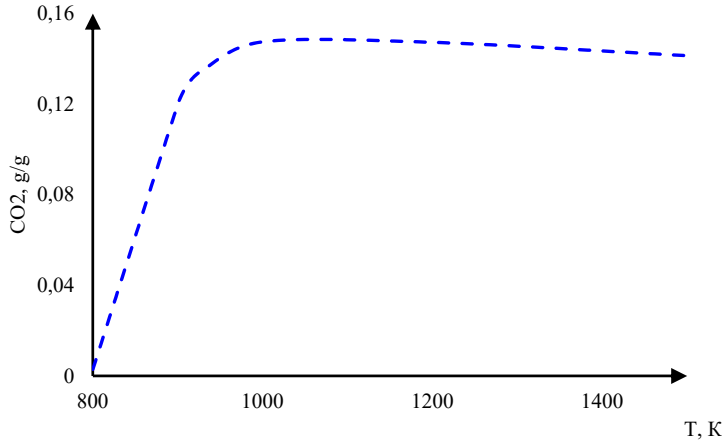

Figure 4 – Dependence of the concentration of the carbon dioxide CO_2 on the initial temperature of the oxidizer during the dodecane combustion

It confirmed this conclusion by three-dimensional graphs of the distribution of the main parameters describing the processes of breakup, dispersion and combustion of liquid fuel (dodecane), which are given below.

Figures 5-9 show the results of the computational experiments on the influence of the oxidizer temperature on the spray and combustion processes of the liquid fuel (dodecane). These graphs were obtained at the optimum oxidizer temperature in the combustion chamber equal to 900 K.

Figure 5 shows the temperature distribution in the combustion chamber for dodecane at time t=2.5 ms at an initial oxidizer temperature of 900 K and at optimal pressure and mass values. From these graphs, we can see how the temperature in the combustion chamber changes at a time. As seen from Figure 5 a, during the dodecane combustion, the region of maximum temperatures at time t=2.5 ms reaches 3.6 cm along the height of the combustion chamber, the rest of the chamber heats to 1000 K. The maximum temperature in the flame is 1526 K at this time of moment (Figure 5 a).

Figure 5 b shows a similar temperature distribution of dodecane at time t=3 ms. When a mixture of fuel vapors with an oxidizer ignites, the fuel (dodecane) burns quickly. A large part of the chamber is covered in a torch across the width (Figure 5 b). When dodecane burns, the maximum temperature is 2080 K (Figure 5 b), i.e. the dodecane's torch has high temperatures, which confirms the results shown in Figure 3.

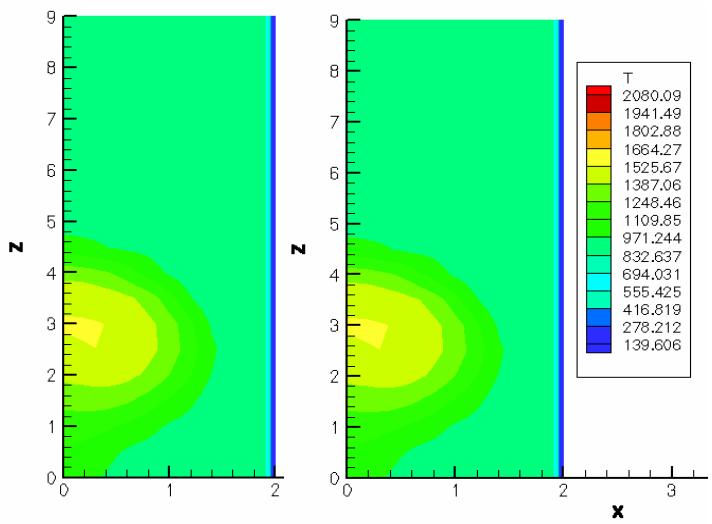

a) t=2.5 ms b) t=3 ms

Figure 5 – Distribution of the temperature in the combustion chamber for dodecane at different times

Figures 6a and 6b show the graphs of the distribution of liquid fuel injection droplets at the optimum temperature at different times. At the moment of time t=2.5 ms, dodecane drops are concentrated in a small region along the width of the combustion chamber. During the combustion of dodecane at the time t=2.5 ms, the liquid fuel droplets reach 0.4 cm along the chamber height (Figure 6 a).

Figure 6b shows the dispersion and temperature distribution of droplets for the dodecane in the combustion chamber at the initial optimum temperature at time t=3 ms. Dodecane droplets lie at a height of 0.52 cm. Fuel droplets are evenly distributed over the height and width of the combustion chamber. In this case, more drops with high temperatures are observed and the maximum temperature of its drops reaches 638.35 K (Figure 6b).

Figure 7 shows the change the dodecane vapor concentration at the time t=2.5 ms at the initial oxidizer temperature equal to 900 K and at the optimal pressure and mass values.

At high turbulence, the area occupied by the fuel in the chamber decreases, which is consistent with the results of Figure 5 and 6. At this time, on the axis of the chamber during the combustion of dodecane, fuel vapors rise to 3.8 cm along the height of the combustion chamber. In the rest of the chamber, the concentration of fuel vapors is minimal.

As can it be seen in the Figure 7, dodecane burns without residue, fuel vapor is almost zero. The minimum concentration of dodecane vapor at a time of 4 ms was 0.01 g/g.

Figures 8-9 show the results of numerical simulations of the distribution of combustion products and oxygen concentration on the chamber axis. The graphs of the distribution of the reaction products at the time instant of 3 ms are shown. So in Figure 8, we can observe how the oxygen concentration in the combustion chamber changes at a time of 3 ms during the initial oxidizer temperature of 900 K and we can say that in most of the combustion chamber at the temperature of 900 K, the oxygen concentration is highest.

The maximum oxygen concentration during the combustion of dodecane is equal to 0.1875 g/g. However, the core of the torch, where the oxidant is consumed for fuel combustion, contains the smallest amount of oxygen: during the combustion of dodecane, the oxidant concentration is 0.05 g/g. When dodecane was burning, the oxygen consumption for fuel combustion was carried out at a height of 3.8 cm to 4.6 cm. Analyzing this graph, one can make sure that the largest amount of oxygen is concentrated in the torch core during the combustion of the liquid fuel.

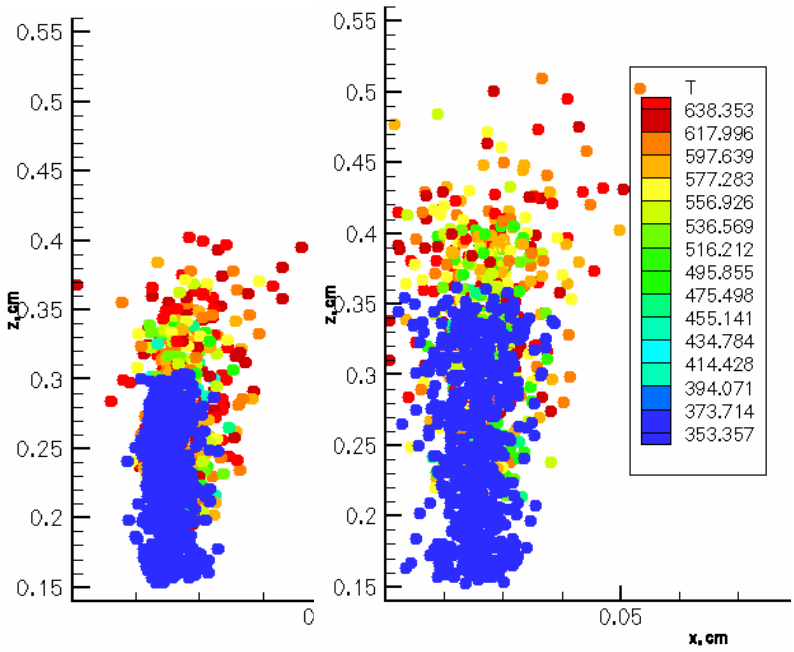

a) t=2.5 ms b) t=3 ms

Figure 6 – Distribution of temperature of the dodecane droplets in the combustion chamber

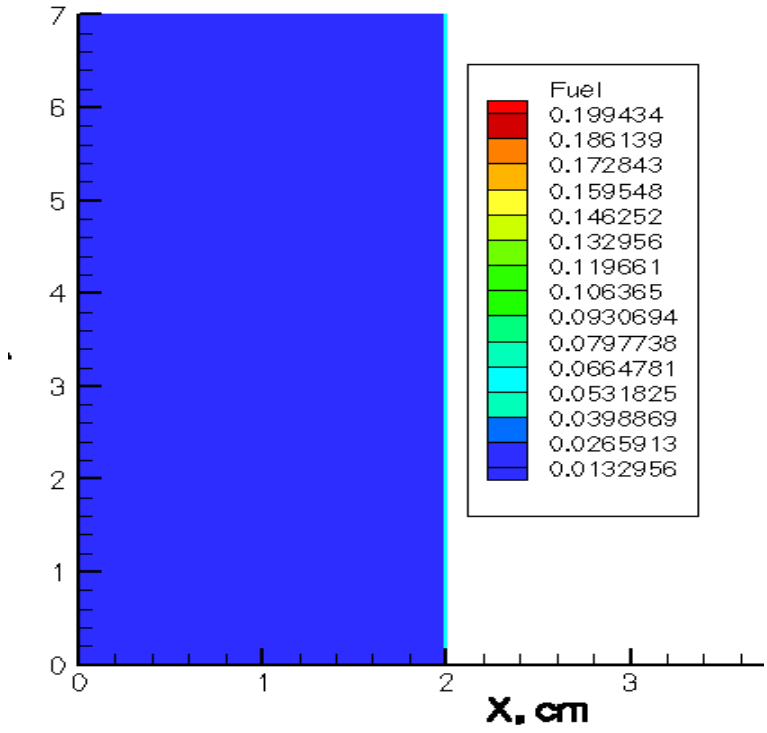

Figure 7 – Concentration field of the fuel vapor at t=2.8 ms

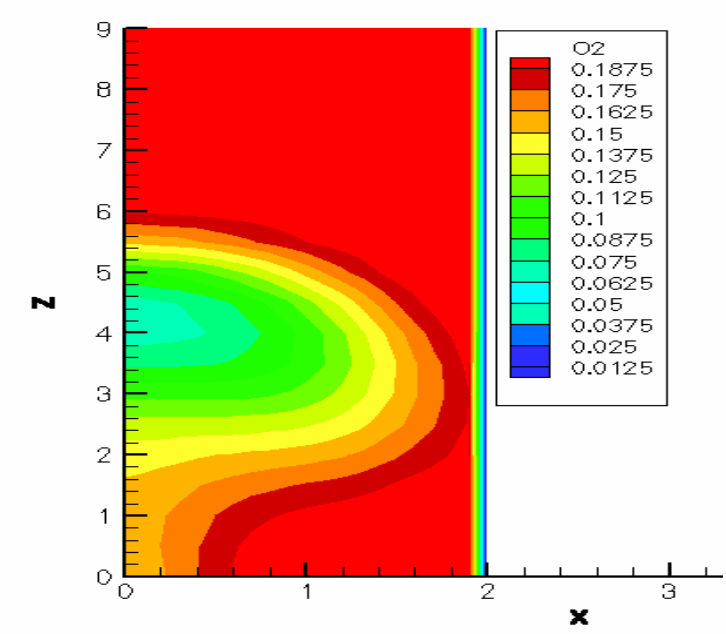

Figure 8 – Concentration field of the oxidizer O_2 in the combustion chamber at the time t=3 ms

Figures 9 and 10 show the graphs of the distribution of the concentrations of water and carbon dioxide at time t=3 ms for dodecane at an initial oxidizer temperature of 900 K and at optimal pressure (80 bar) and mass (7 mg). Analysis of Figure 9 shows that at a time of 3 ms, the maximum concentration of water resulting from the chemical reaction of dodecane combustion reached a value of 0.060256 g/g. In the remaining parts of the combustion chamber, the concentration of water reaches its lowest value, in most part of the combustion chamber, the minimum amount of moisture is maintained, which is equal to 0.00306837 g/g.

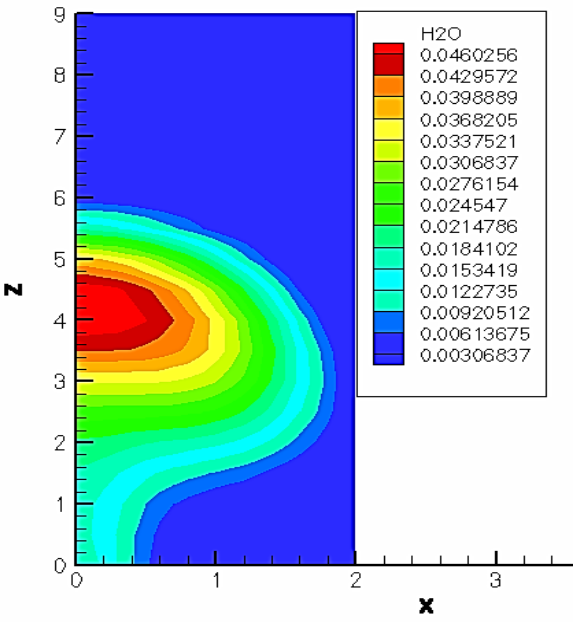

Figure 9 – Distribution of water vapor H_2O during the combustion of dodecane in the combustion chamber at t=3 ms

Figure 10 shows the results of numerical modeling of the formation of carbon dioxide during the combustion of dodecane at an optimal temperature of 900 K. Analysis of the figure shows that the maximum amount of carbon dioxide for dodecane on the axis of the combustion chamber, the concentration of carbon dioxide reaches a value equal to 0.103878 g/g. At the exit from the combustion chamber, the concentration of carbon dioxide decreases and takes on minimum values. So, for dodecane at an optimal temperature of 900 K, the concentration of carbon dioxide is 0.008 g/g.

Numerical simulation data were compared with the probability density function of droplet size distribution. At a distance of 40 mm from the injector nozzle at the center of one separate jet, this function is in good agreement with both experimental data and the results of numerical simulation.

Experimental [28-32] and numerical droplet size distributions were compared with two standard particle distribution functions that are often found in the technical literature. The first is the log normal distribution, and the second is the Rosin-Rammler distribution (Figure 11).

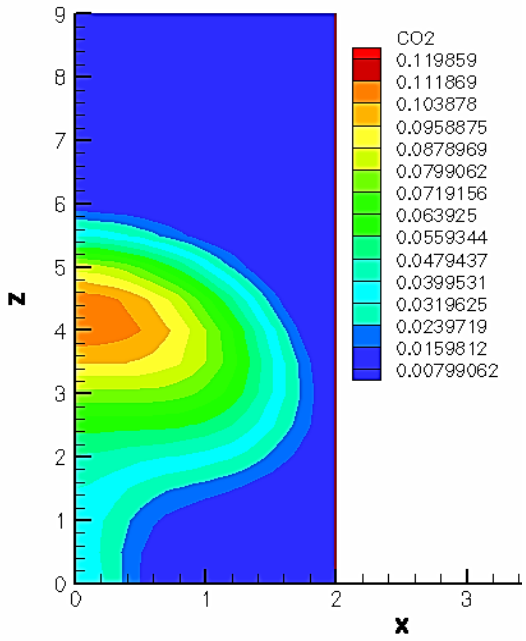

Figure 10 – Distribution of carbon dioxide CO_2 concentrations during the combustion of dodecane at t=3ms

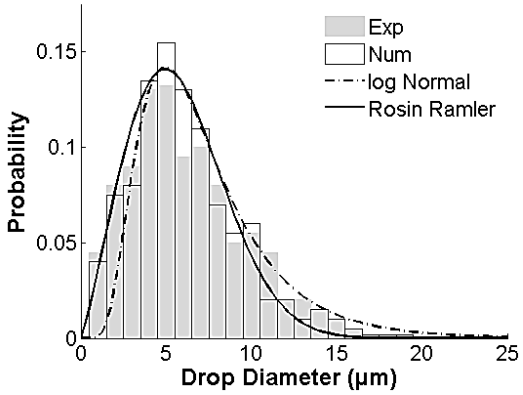

Figure 11 – Comparison of the probability function of droplet size distribution with experimental and numerical data

In the experiment, we observed a time delay of 400 ms when the injector was switched on electrically and physically. This deceleration comprises an electrical and hydraulic time delay. This deceleration was considered in the numerical simulation so that the start time of fuel injection was identical to the experiment.

5 Conclusions

In this way, we presented the numerical study of the influence of the initial temperature of the oxidant on the combustion of dodecane in this article. The optimal parameters for the fuel mass and pressure in the combustion chamber, which was previously determined in [23-27] have been used. It was shown that for the investigated type of fuel (dodecane), the best initial temperature of the oxidizer in the combustion chamber is 900 K. At this temperature, the fuel burns completely, the chamber heats to sufficiently high temperatures, and the concentration of the resulting carbon dioxide takes the lowest values.

Verification of the results obtained during computational experiments, comparison with experimental data and theoretical calculations, showed good agreement. This allows us to conclude that the mathematical model proposed in this work, which describes the breakup, dispersion, evaporation and combustion of liquid fuel injected into the combustion chamber at high turbulence, can be further used to study the processes of heat and mass transfer during multi-hole injection.

Obtained results can be used in the design of various internal combustion engines, which would simultaneously solve the problem of optimizing the combustion process, increasing the efficiency of fuel combustion and minimizing harmful emissions.

Acknowledgments

The Ministry of Education and Science of the Republic of Kazakhstan No. AP08857288 has supported financially this work.

References

1. A. Askarova, et al. Computational method for investigation of solid fuel combustion in combustion chambers of a heat power plant // High Temperature. – 2015. – Vol. 53. – P. 751-757. https://doi.org/10.1134/S0018151X15040021

2. V. Messerle, et al. Processes of heat and mass transfer in furnace chambers with combustion of thermochemically activated fuel // Thermophysics and Aeromechanics. – 2019. – Vol. 26. – P. 925-937. https://doi.org/10.1134/S0869864319060143

3. P. Safarik, et al. Optimization of the solid fuel combustion process in combustion chambers in order to reduce harmful emissions // News of the national academy of sciences of the Republic of Kazakhstan. Physical and mathematical series. – 2019. – Vol. 6. – p. 34-4. https://doi.org/10.32014/2019.2518-1726.71

4. Z. Gabitova, et al. Simulation of the aerodynamics and combustion of a turbulent pulverized-coal flame // 4th International Conference on Mathematics and Computers in Sciences and in Industry (MCSI 2017). – 2017. – Vol. 17668480. – P. 92-97. https://doi.org/10.1109/MCSI.2017.23

5. P. Safarik, A. Nugymanova, et al. 3D modeling of heat transfer processes in the combustion chamber of a TPP boiler // News of the national academy of sciences of the Republic of Kazakhstan. Physical and mathematical series. – 2019. – Vol. 6. – P. 5-13. http://dx.doi.org/10.32014/2019.2518-1726.68

6. A. Askarova, et.al. Numerical research of aerodynamic characteristics of combustion chamber BKZ-75 mining thermal power station // Procedia Engineering. – 2012. – Vol. 42. – P. 1250-1259. https://doi.org/10.1016/j.proeng.2012.07.517

7. M.M. Khan, J. Helie, M. Gorokhovski Computational methodology for non-evaporating spray in quiescent chamber using Large Eddy Simulation // International Journal of Multiphase Flow. – 2018. – Vol. 102. – P. 102-118. https://doi.org/10.1016/j.ijmultiphaseflow.2018.01.025

8. V. Messerle. A. Ustimenko, et al. Reduction of noxious substance emissions at the pulverized fuel combustion in the combustor of the BKZ-160 boiler of the Almaty heat electro power station using the "Overfire Air" technology // Thermophysics and Aeromechanics. – 2016. – Vol. 23. – P. 125-134. http://dx.doi.org/10.1134/S0869864316010133

9. A. Bekmuhamet, et al. Mathematical simulation of pulverized coal in combustion chamber // Procedia Engineering. – 2012. – Vol. 42. – P. 1150-1156. https://doi.org/10.1016/j.proeng.2012.07.507

10. S. Bolegenova, Z. Gabitova, et al. Control harmful emissions concentration into the atmosphere of megacities of Kazakhstan Republic // IERI Procedia. – 2014. – Vol. 10. – P. 252-258. https://doi.org/10.1016/j.ieri.2014.09.085

11. A. Takeishi Knowledge Partitioning in the Interfirm Division of Labor: The Case of Automotive Product Development // Organization Science. – 2002. – Vol. 13. – P. 321-338. https://doi.org/10.1287/orsc.13.3.321.2779

12. C. Wang, J. Chen, J. Zou Decomposition of energy-related CO_2 emission in China: 1957–2000 // Energy. – 2005. – Vol. 30. – P. 73-83. https://doi.org/10.1016/j.energy.2004.04.002

13. P. Safarik, et al. Numerical investigation of heat and mass transfer processes in the combustion chamber of industrial power plant boiler. Part 1. Flow field, temperature distribution, chemical energy distribution // Applied and Computational Mechanics. – 2017. – Vol. 11. – P. 115-128. http://dx.doi.org/10.24132/acm.2017.395

14. P. Safarik, et al. Investigation of heat and mass transfer processes in the combustion chamber of industrial power plant boiler. Part 2. Distribution of concentrations of O_2, CO, CO_2, NO // Journal of Applied and Computational Mechanics. – 2018. – Vol. 12. – P. 127-138. http://dx.doi.org/10.24132/acm.2018.396

15. D. Gao, N. Morley, V. Dhir Numerical simulation of wavy falling film flow using VOF method // Journal of Computational Physics. – 2003. – Vol. 192. – P. 624-642. https://doi.org/10.1016/j.jcp.2003.07.013

16. A. Askarova, et al. 3D-modelling of Kazakhstan low-grade coal burning in power boilers of thermal power plant with application of plasma gasification and stabilization technologies // Journal of Physics: Conference Series. – 2019. – Vol. 126. – P. 12-22. http://dx.doi.org/10.1088/1742-6596/1261/1/012022

17. E. Villermaux Mixing and spray formation in coaxial jets // Journal of propulsion and power. – 1998. – Vol. 14, Issue 5. – P. 807-817. http://dx.doi.org/10.2514/2.5344

18. J.C. Lasheras, E.J Hopfinger Liquid jet instability and atomization in a coaxial gas stream // Annual Review of Fluid Mechanics. – 2000. – Vol. 32, Issue 1. – P. 275-308. https://doi.org/10.1146/annurev.fluid.32.1.275

19. B. Rongshan, et al. Research on the CFD numerical simulation of flash boiling atomization // Energy. – 2018. – Vol. 165. – P. 768-781. https://doi.org/10.1016/j.energy.2018.09.143

20. P. Wang P, J. Fröhlich, V. Michelassi, W. Rodi Large-eddy simulation of variable-density turbulent axisymmetric jets // International Journal of Heat and Fluid Flow. – 2008. – Vol. 29, Issue 3. – P. 654-664. http://dx.doi.org/10.1016/j.ijheatfluidflow.2008.02.002

21. M. Gorokhovski, J. Jouanguy, A. Chtab-Desportes Stochastic model of the near-to-injector spray formation assisted by a high-speed coaxial gas jet // Fluid Dynamics Research. – 2009. – Vol. 41, Issue 3. – P. 15. http://dx.doi.org/10.1088/0169-5983/41/3/035509

22. M. Gorokhovski, M. Herrmann Modeling primary atomization // Annual Review of Fluid Mechanics. – 2008. – Vol. 40. – P. 343-366. https://doi.org/10.1146/annurev.fluid.40.111406.102200

23. A. Askarova, et al. Stochastic simulation of the spray formation assisted by a high pressure // AIP Conference Proceedings. – 2010. – Vol. 1207. – P. 66-73. https://doi.org/10.1063/1.3366446

24. S. Bolegenova, Sh. Ospanova, et al. Investigation of various types of liquid fuel atomization and combustion processes at high turbulence // Journal of Engineering and Applied Sciences. – 2018. – Vol. 13. – P. 4054-4064. http://dx.doi.org/10.36478/jeasci.2018.4054.4064

25. M. Gorokhovski, V. Saveliev Analyses of Kolmogorov's model of breakup and its application into Lagrangian computation of liquid sprays under air-blast atomization // Physics of Fluids. – 2003. – Vol. 15. – P. 184-192. http://dx.doi.org/10.1063/1.1527914

26. M. Gorokhovski, J. Helie, et al. Experimental and numerical study of flash boiling in gasoline direct injection sprays //Applied Thermal Engineering. – 2017. – Vol. 123. – P. 377-389. https://doi.org/10.1016/j.applthermaleng.2017.05.102

27. C. Arcoumanis, M. Gavaises, E. Giannadakis Modelling of cavitation in diesel injector nozzles // Journal of fluid mechanics. – 2008. – Vol. 616. – P. 153-193. http://dx.doi.org/10.1017/S0022112008003777

28. A. Wehrfritz, et al. Large Eddy Simulation of high-velocity fuel sprays: studying mesh resolution and breakup model effects for spray A // Atomization and Sprays. – 2013. – Vol. 23. – P. 419-442. http://dx.doi.org/10.1615/AtomizSpr.2013007342

29. M. Mojtabi, G. Wigley, J. Helie The effect of flash boiling on the atomization performance of gasoline direct injection multistream injectors // Atomization and Sprays. – 2014. – Vol. 24. – P. 467-493. http://dx.doi.org/10.1615/AtomizSpr.2014008296

30. M. Zhang, M. Xu, Y. Zhang, W. Zeng Flow field evaluation of superheated fuel sprays using high-speed PIV // SAE Technical Papers. – 2011. – P. 1880-1890. https://doi.org/10.4271/2011-01-1880

31. G. Zhang, et al. Macroscopic characterization of flash-boiling multi-hole sprays using planar laser induced exciplex fluorescence technique. Part I. On-axis spray structure // Atomization and Sprays. – 2012. – Vol. 22. – P. 861-878. http://dx.doi.org/10.1615/AtomizSpr.2013006760

32. W. Zeng, et al. Laser sheet drop sizing of evaporating sprays using simultaneous LIEF/MIE techniques // Proceedings of the Combustion Institute. – 2013. – Vol. 34. – P. 1677-1685. https://doi.org/10.1016/j.proci.2012.07.061

IRSTI 29.27.07 https://doi.org/10.26577/phst.2021.v8.i2.05

Influence of an external electric field on plasma parameters around an isolated dust particle

A. Fedoseev[1,*], M. Salnikov[2] and G. Sukhinin[2]

[1] Joint Institute for High Temperatures RAS, Izhorskaya st. 13 Bd.2, 125412, Moscow, Russia
[2] Institute of Thermophysics SB RAS, 1, Lavrentyev Ave., 630090, Novosibirsk, Russia
[*]e-mail: alex.fed245@gmail.com

The paper presents new numerical results on the behavior of plasma parameters around an isolated charged dust particle under the action of the external electric field. For the first time, the model takes into account the dependence of mean electron energy on the reduced electric field strength. As a result of the calculations, the dependencies of self-consistent spatial distributions of the electron and ion densities and electric potential around the dust particle on reduced external electric field strength were obtained. These distributions were analyzed through the expansion into Legendre polynomials. The processes of ion focusing and wake formation behind the dust particle were studied. The dust particle charge and the dipole moment of the "ion cloud - dust particle" are calculated for different values of the reduced electric field and ion mean free paths. It is shown that in the determination of electron density spatial profile and the dust particle charge the dependence of electron temperature on electric field strength plays a significant role.

Key words: dusty plasma, dust particle charging, dipole moment, wake, plasma polarization.
PACS number(s): 52.27.Lw, 52.35.Tc, 52.20.−j

1 Introduction

Dusty or complex plasma is a new field of plasma physics studding the interaction of solid micron-sized particles immersed into typical low-temperature plasma (see e.g. recent reviews [1,2]). Many different phenomena associated with the dusty plasma have been studied experimentally and numerically: dust grains charging [3], the formation of crystalline and liquid structures [4,5], phase transitions between these structures [5,6], dust-acoustic waves [7], the orientation of non-spherical dust particles in a discharge [8], and many others.

It is well known that in streaming plasma or in an external electric field the pseudo-periodic oscillating structures in electric potential and ion density arise behind a dust particle [18,19,20]. These phenomena are responsible for the dust particles ordering. Such a periodic structure is called a wake, and is a consequence of ion focusing behind the dust grain. The most popular approaches for studying wakes are PIC [9-11] and LR [12,13] numerical methods.

In previous works [14-19], the behavior of plasma parameters around an isolated charged dust particle under the action of the external electric field was studied. As a result of the calculations, the dependencies of self-consistent spatial distributions of the electron and ion densities and electric potential around the dust particle on reduced external electric field strength were obtained. The processes of ion focusing and wake formation behind the dust particle were studied. The dust particle charge and the dipole moment of the "ion cloud – dust particle" are calculated for different values of dust particles size, electric field strength and ion mean free paths. However, in all these studies the parameter $\tau = T_e/T_i$, i.e. the ratio of electron and ion temperatures, was the constant parameter (typically $\tau = 100$), which did not depend on the external electric filed. It is well known that the electron mean energy is a function of the reduced electric field specific for the type of a buffer gas. In present work, the dependence of mean electron energy on the reduced electric field was taken into account for the first time.

2 Model

A detailed description of the numerical model used for the calculation of the plasma parameters around an isolated dust particle was presented

elsewhere [14-19]. Let us just remind the following points. The geometry of the computational domain was taken as a parallelepiped. An impenetrable sphere of radius $r_0 << \lambda_i$ placed in the center of this domain plays the role of the solid dust particle, where λ_i is the ion Debye length.

To start the calculations, an ion is generated with the random coordinates and velocities. The speed of ions is taken according to the Maxwell distribution. Newton's motion equations were used to calculate the trajectory of this generated ion. In these equations, the action of electric field induced by the charged dust particle and external electrostatic field on the ion trajectory is taken into account. During its movement the ion could either fall on a dust particle or fly away the computational domain or collide with a neutral atom.

The modeling domain was subdivided into cells (i,j) according to cylindrical coordinates ρ and z, respectively. The volume of each cell is determined by:

$$V_{i,j} = 2\pi\rho_i \Delta\rho_i \Delta z_j \tag{1}$$

During ion traveling through the cell (i,j), the time $T_{i,j}$, which the ion spent in this cell, is accumulated. Then, this time is normalized to the volume of the cell $V_{i,j}$. The obtained value is summed up with the already accumulated time statistics for this cell:

$$n_i(i,j) = n_i(i,j) + \frac{T_{i,j}}{V_{i,j}}. \tag{2}$$

We use the dimensionless parameters in the calculations, i.e. the dimensionless charge of the dust particle Q' and the dimensionless external electric field E' given by the expressions:

$$Q' = \frac{e^2 Z_d}{\lambda_i k T_i}, \quad E' = \frac{eE\lambda_i}{kT_i} \tag{3}$$

At the beginning of calculations, the following spatial distribution of the electric potential was used:

$$U_0(\rho,z) = -\frac{Q'}{r}\exp(-r) - \\ -E'z, \quad r = \sqrt{\rho^2 + z^2} \tag{4}$$

From the statistics obtained for every cell, the dimensionless distribution of space charge $n(\rho,z)$, is calculated:

$$n(\rho,z) = \frac{n_i(\rho,z) - n_e(\rho,z)}{n_\infty}, \tag{5}$$

were n_∞ is the plasma density far from the dust particle. The spatial distribution of electron density n_e is assumed to be equal to the Boltzmann distribution $n_e(\rho,z) = n_\infty \exp(U(\rho,z)/(kT_e))$.

The self-consistent spatial distribution of electric potential in the system is then calculated as:

$$U(\rho,z) = -\frac{Q'}{r} + \\ + \iiint_{V_{syst}} \frac{n(\rho',\phi',z')\rho' d\rho' d\phi' dz'}{\left|\vec{r} - \vec{r}\,'\right|}, \tag{6}$$

The general iterative scheme for calculation of a steady state self-consistent solution for all plasma parameters is as follows:

1) The calculation of ion trajectories under the action of the spatial distribution of electric potential (6). After the ion collides with the neutral atom or fall onto the dust particle surface, a new ion is simulated. The statistics is accumulated for all ions.

2) The distribution of the space charge (5) is determined and the self-consistent electric potential of the system is calculated (6). The charge of the dust particle is calculated from the condition that the flows of ions and electrons to its surface are equal to each other.

3) The iterative procedure is repeated until the full convergence of all spatial distributions, including the charge of the dust particle.

For small values of the external electric field, the spatial distributions of electron density $n_e(r,\theta)$, ion density $n_i(r,\theta)$ and electric potential $U(r,\theta)$ weakly deviate from spherical symmetric (r and θ are spherical coordinates). In this case, $U(r,\theta)$ can be determined through the expansion of the space charge distribution $n(r,\theta)$ into the Legendre polynomials (spherical harmonics):

$$n(r,\theta) = n_i(r,\theta) - n_e(r,\theta) = \\ = \sum_{k=0} n_k(r) P_k(\cos\theta), \tag{7}$$

where

$$n_k(r) = \frac{2k+1}{2}\int_0^{\pi} n(r,\theta)P_k(\cos\theta)\sin\theta d\theta \,. \quad (8)$$

It should be noted that the zero isotropic term of the expansion, $n_0(r)$, determines the plasma charge around the dust particle:

$$Q_{pl} = \frac{1}{2}\int_0^{\infty}\int_0^{\pi} n(r,\theta)r^2\sin\theta d\theta dr = \int_0^{\infty} n_0(r)r^2 dr \,, \quad (9)$$

and the first isotropic term of the expansion, $n_1(r)$, determines the dipole moment of a "dust particle – ion cloud" system:

$$P_{pl} = \frac{1}{2}\int_0^{\infty}\int_0^{\pi} n(r,\theta)r^3\cos\theta\sin\theta d\theta dr = \frac{1}{3}\int_0^{\infty} n_1(r)r^3 dr. \quad (10)$$

3 Results

In calculations, a spherical dust particle of radius r_0 = 1 μm is considered. Ion temperature is assumed to be equal to the room temperature, i.e. kT_i = 0.03 eV, $T_i = T_g$. The ion Debye length is set to be $\lambda_i = 10^{-2}$ cm, i.e. $r_0 = 10^{-2}\ \lambda_i$. Ion mean free path for the resonant charge exchange collisions with neutrals (argon) is taken in the interval l_i = 2.5-10 λ_i. The interval of external electric field values is $E' = 0 - 0.6$, i.e. $E = 0 - 1.5$ V/cm. The gas (argon) density $n_0 = 1/(2^{1/2}\sigma l_i)$ is determined by the ion mean free path l_i and the resonant charge exchange collision cross section σ (for argon [20]).

In the previous authors works as well as in other literature, the parameter $\tau = T_e/T_i$ was the given parameter, where T_e is the electron temperature. In this paper, we take into account that electron temperature is the function of the reduced external electric field E/N. We use the dependence of the electron mean energy $\langle\varepsilon\rangle = 3/2kT_e$ versus reduced electric field E/N calculated with the help of BOLSIG+ solver [21] (see Figure 1) to obtain the dependence $T_e(E/N)$. This dependence plays significant role in the determination of electron density spatial profile and of electron flux towards the dust particles, i.e. influences the dust particle charge.

Figure 2 presents the dependence of the particle charge on electric field strength both in dimensionless and dimension forms. The aim of the calculations is to determine the role of the ion mean free path l_i on the dust particle charge at the same electron temperature. It is seen that different curves for different ion mean free paths substantially differ from each other (40%). The dust particle charge and charge number increase almost linearly with the electric field strength excepting the region of low electric filed, i.e. the low electron temperature. It should be noted that at constant parameter τ considered in previous papers the charges differ more slightly.

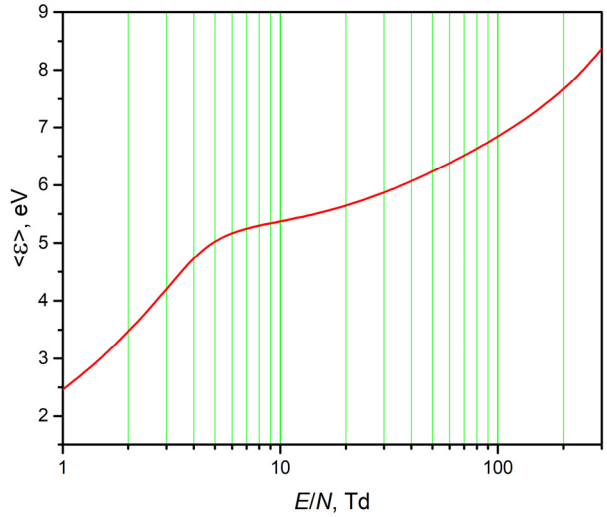

Figure 1 – Electron mean energy <ε> versus reduced electric field E/N [21]

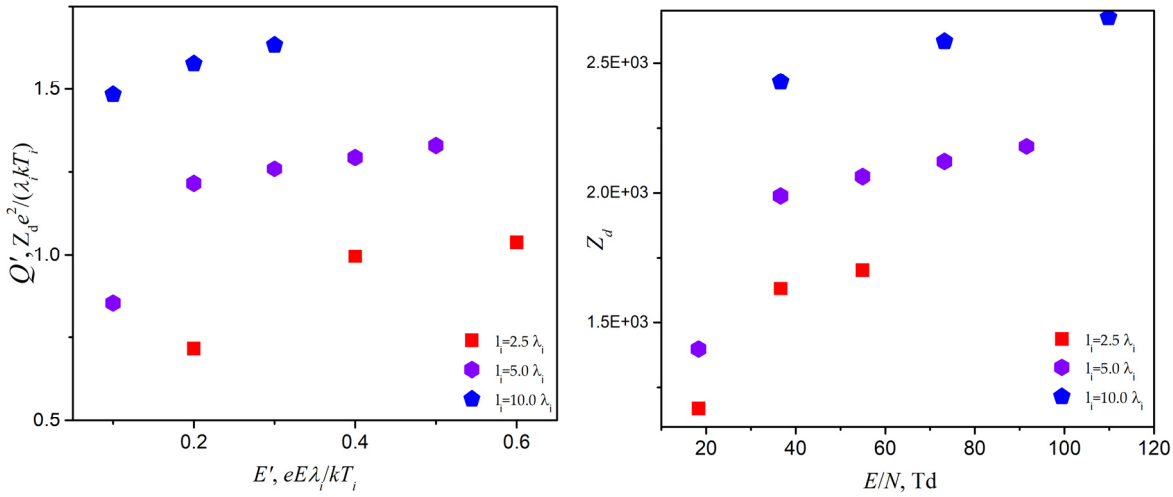

Figure 2 – Dimensionless dust particle charge Q' versus dimensionless electric field E' (left figure) and dust particle charge number Z_d versus reduced electric field E/N (right figure) for different values of ion mean free paths

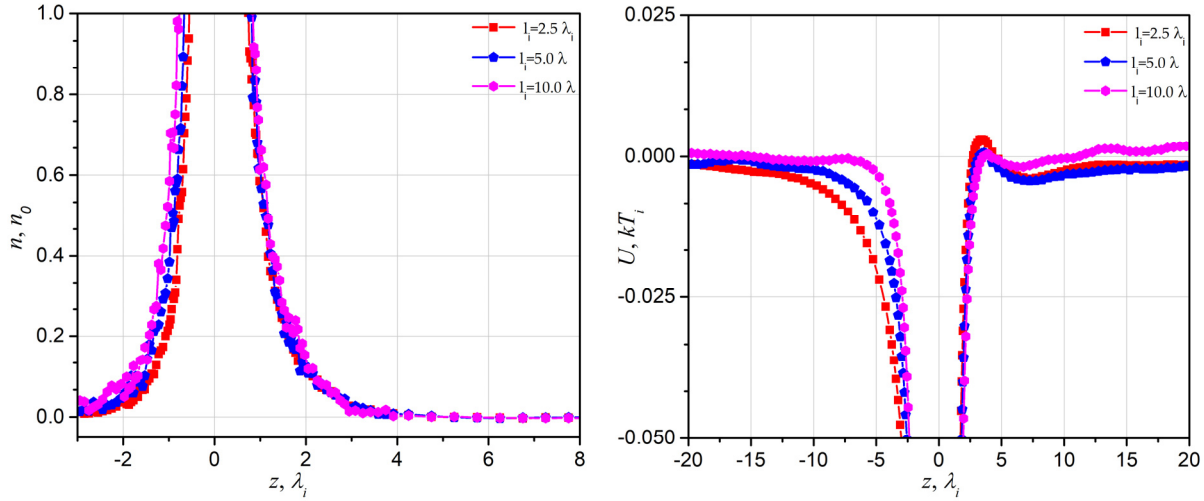

Figure 3 – The sections of the spatial distributions of the space charge density $n(z,\rho=0)$ (left figure) and the electric potential $U(z,\rho=0)$ (right figure) for different values of ion mean free paths. Reduced electric field E/N = 37 Td

Figure 3 shows sections ($\rho=0$) of the longitudinal distributions of the space charge density $n(z,\rho=0)$ and the electric potential $U(z,\rho=0)$. The value of the reduced electric field strength for all curves is the same E/N = 37 Td. It is interesting to note that the right parts of the space charge density and the electric potential are substantially deviate for different ion mean free paths and the right parts are almost coincide with each other. Thus, the wakes are formed almost at the same distances. The more the ion mean free path the more amplitude of the oscillations of the electric potential behind the dust particle due to the fact that the collisions of ions with neutrals destruct the wakes.

Figure 4 presents radial distributions of zero and first harmonics multiplied by special compounds, i.e. functions $n_0(r)r^2/Q'$ and $n_1(r)r^3 l_i^{1/2}$. The result for $n_0(r)r^2/Q'$ shows that at different electron energies the shape of the charge distribution is uniform. This is very interesting taking into account that the case for l_i = 2.5 has a strongly narrowed ion cloud. The result for $n_1(r)r^3 l_i^{1/2}$ is also interesting and shows that the

unscreened part (closer to the particle than $3\lambda_i$) behaves like a functional from the root of the l_i. The area beneath function $n_1(r)r^3$ multiplied by the $l_i^{1/2}$ is equal for different l_i (see Figure 5).

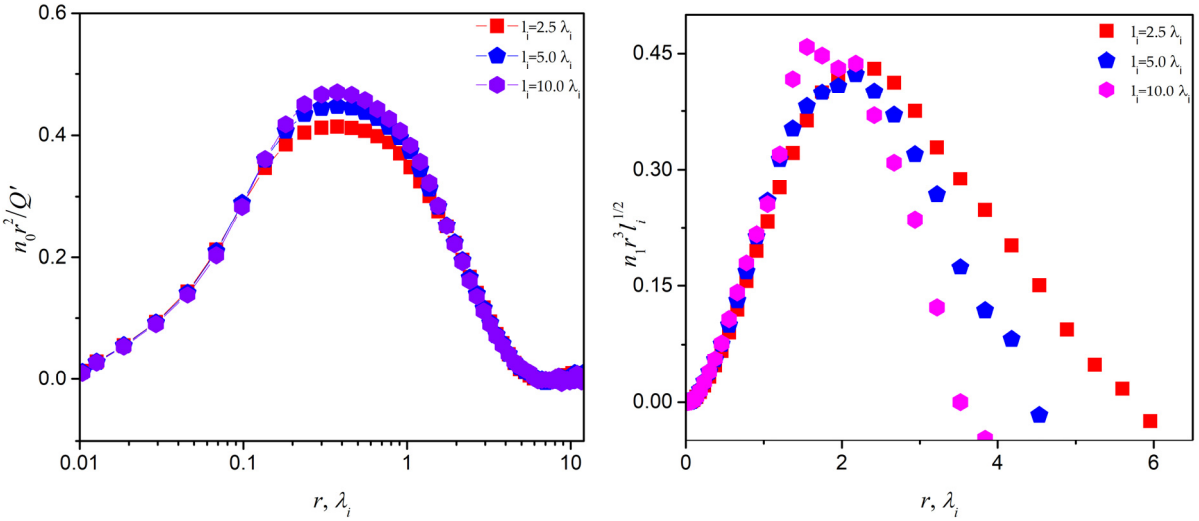

Figure 4 – Functions $n_0(r)r^2/Q'$ (left figure) and $n_1(r)r^3l_i^{1/2}$ (right figure) for different values of ion mean free paths. Reduced electric field E/N = 37 Td

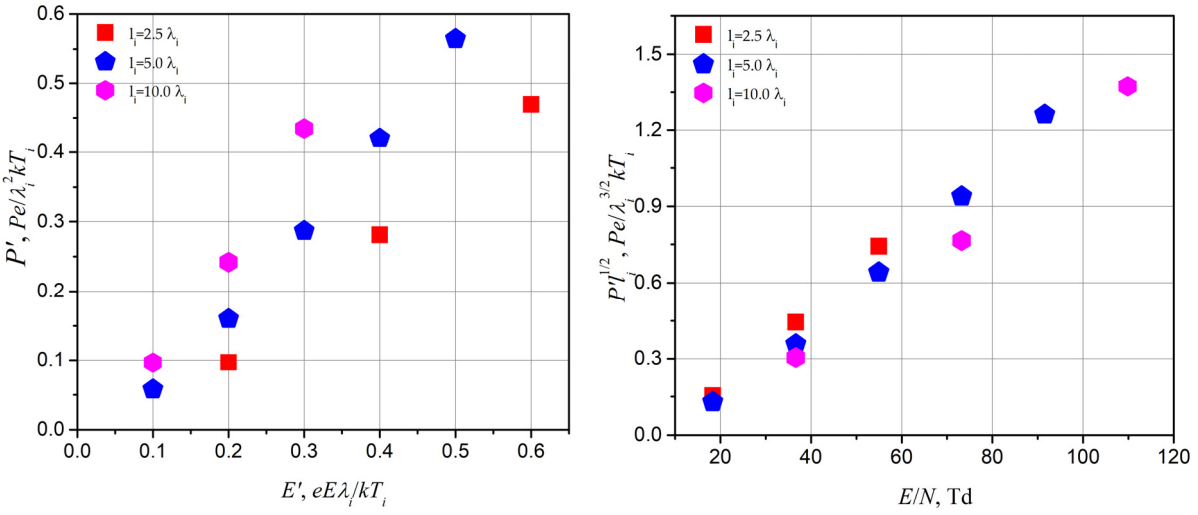

Figure 5 – Dimensionless dipole moment versus dimensionless electric field (left figure) and function $P'l_i^{1/2}$ versus reduced electric field E/N for different values of ion mean free paths

The dipole moment of the "dust particle – ion cloud" ought also be reviewed for the same electron energy for various l_i. The dipole moment P_{pl} is calculated by Equation (10). Figure 5 (left figure) shows the dependence of dimensionless dipole moment P' on dimensionless electric field E' for different ion mean free paths. It is seen that the curves increase almost linearly with the electric field. The more l_i the more value of the dipole moment due to ions could orbit around the particle more time contributing to plasma anisotropy. The dependence of the function $P'l_i^{1/2}$ on the reduced electric filed is presented on the right image of the Figure 5. It is seen that different curves for different l_i are almost coincide with each other.

As a result of this study, it was shown that, despite taking into account the change in the

electron energy, and, as a consequence, the change in the dust particle charge value, the dipole moment can still be characterized as a linear function of the external electric field (as in [17]). Thus, taking into account the electron energy does not affect the dependence of the ion cloud anisotropy on the magnitude of the external field.

4 Conclusions

In the paper the results of the numerical modeling of the plasma parameters around an isolated charged dust particle under the action of an external electric field are presented. Previously developed computational model was expanded by taking into account the dependence of mean electron energy on the reduced electric field strength. As a result of calculations, the dependencies of self-consistent spatial distributions of the electron and ion densities, electric potential around the dust particle were obtained for different values of ion mean free path and reduced electric field. It is shown that the accounting for the dependence of electron temperature on electric field strength plays significant role in the determination of electron density spatial profile and the dust particle charge by means of electron flux towards the dust particle.

References

1 M.Y. Pustylnik, A.A. Pikalev, A.V. Zobnin, I.L. Semenov, H.M. Thomas, O.F. Petrov. (2021) Physical aspects of dust–plasma interactions // Contributions to Plasma Physics. – 2021. – P. e202100126. https://doi.org/10.1002/ctpp.202100126

2 R. Merlino. Dusty plasmas: from Saturn's rings to semiconductor processing devices // Advances in Physics: X. – 2021. – Vol. 6. – Iss. 1. – Pp. 1873859. https://doi.org/10.1080/23746149.2021.1873859

3 G. I. Sukhinin, A. V. Fedoseev. Charging of dust grains in a non-equilibrium plasma of a stratified glow discharge // Plasma Physics Reports. -2007. -Vol. 33. -Iss.12. -Pp. 1023-1031. https://doi.org/10.1134/S1063780X07120070

4 H. Ikezi. Coulomb solid of small particles in plasmas // The Physics of Fluids. – 1986. – Vol. 29. – Iss. 6. – Pp. 1764-1766. https://doi.org/10.1063/1.865653

5 H. M. Thomas, G. E Morfill. Melting dynamics of a plasma crystal // Nature. – 1996. – Vol. 379. – Iss. 6568. – Pp. 806-809. https://doi.org/10.1038/379806a0

6 S. A. Khrapak, B. A. Klumov, P. Huber, V. I. Molotkov, A. M. Lipaev, V. N. Naumkin, A. V. Ivlev, H. M. Thomas, M. Schwabe, G. E. Morfill, O. F. Petrov, V. E. Fortov, Y. Malentschenko, S. Volkov. Fluid-solid phase transitions in three-dimensional complex plasmas under microgravity conditions // Physical Review E. -2012. -Vol. 85. -Iss. 6. -Pp. 066407. https://doi.org/10.1103/PhysRevE.85.066407

7 P. K. Shukla, V. P. Silin. Dust ion-acoustic wave // Physica Scripta. -1992. -Vol.45. -Iss. 5. -Pp. 508-508. https://doi.org/10.1088/0031-8949/45/5/015

8 A. V. Ivlev, A. G. Khrapak, S. A. Khrapak, B. M. Annaratone, G. Morfill, K. Yoshino. Rodlike particles in gas discharge plasmas: Theoretical model // Physical Review E. -2003. -Vol.68. -Iss.2. -Pp. 026403. https://doi.org/10.1103/PhysRevE.68.026403

9 P. Ludwig, W. J. Miloch, H. Kahlert, M. Bonitz. On the wake structure in streaming complex plasmas // New J. Phys. -2012. -Vol.14. -Pp. 053016. https://doi.org/10.1088/1367-2630/14/5/053016

10 I. H. Hutchinson. Nonlinear collisionless plasma wakes of small particles // Phys. Plasmas. -2011. -Vol. 18. -Pp. 032111. https://doi.org/10.1063/1.3562885

11 I. H. Hutchinson. Intergrain forces in low-Mach-number plasma wakes // Phys. Rev. E. -2012. -Vol. 85, -Pp. 066409. https://doi.org/10.1103/PhysRevE.85.066409

12 R. L. Dewar., D. Leykam. Dressed test particles, oscillation centres and pseudo-orbits // Plasma Phys. Control. Fusion. -2012. -Vol. 54. -Pp. 014002. https://doi.org/10.1088/0741-3335/54/1/014002

13 R. Kompaneets, G. E. Morfill, A. V. Ivlev. Interparticle attraction in 2D complex plasmas // Phys. Rev. Lett. -2016. -Vol. 116. -Pp. 125001. https://doi.org/10.1103/PhysRevLett.116.125001

14 G.I. Sukhinin, A.V. Fedoseev, M.V. Salnikov. Polarization of a dust particle and surrounded plasma in an external electric field // Contrib. Plasma Phys, -2016. -Vol. 56. -No. 5. -Pp. 397-402. https://doi.org/10.1002/CTPP.201500128

15 G. I. Sukhinin, A. V. Fedoseev, M. V. Salnikov, A. Rostom, M. M. Vasiliev, O. F. Petrov. Plasma anisotropy around a dust particle placed in an external electric field // Phys. Rev. E. -2017. -Vol. 95. -Pp. 063207. https://doi.org/10.1103/PhysRevE.95.063207

16 G.I. Sukhinin, A.V. Fedoseev, M.V. Salnikov, A. Rostom. Plasma polarization and wake formation behind a dust particle in an external electric field // IEEE Transactions on Plasma Science. – 2018. – Vol. 46. – No. 4. – Pp. 749-754. https://doi.org/10.1109/TPS.2017.2775656

17 G.I. Sukhinin, A.V. Fedoseev, M.V. Salnikov. Effect of ion mean free path length on plasma polarization behind a dust particle in an external electric field // Contributions to Plasma Physics. -2019. -Pp. e201800152. https://doi.org/10.1002/CTPP.201800152

18 G.I. Sukhinin, A.V. Fedoseev, M.V. Salnikov. The influence of dust particle geometry on its charge and plasma potential // Contributions to Plasma Physics. -2019. -Pp. e201800153. https://doi.org/10.1002/ctpp.201800153

19 G. Sukhinin, M. Salnikov, A. Fedoseev. Plasma anisotropy around non-spherical conductive dust particle. Physical Sciences and Technology. -2019. -Vol. 6. -No.2. -Pp. 37-43. https://doi.org/10.26577//phst-2019-2-p5

20 S.A. Maiorov. Ion drift in a gas in an external electric field // Plasma Phys. Rep. -2009. -Vol. 35. -Pp. 802-812. https://doi.org/10.1134/S1063780X09090098

21 G. J. M. Hagelaar, L. C. Pitchford. Solving the Boltzmann equation to obtain electron transport coefficients and rate coefficients for fluid models // Plasma Sources Sci. Techn. -2005. -Vol.14. -Pp. 722-733. https://doi.org/10.1088/0963-0252/14/4/011

IRSTI 41.21.05; 41.21.19 https://doi.org/10.26577/phst.2021.v8.i2.07

Detecting the Sun's active region using image processing techniques

A. Sarsembayeva[1,*], M. Odsuren[2,†], F. Belisarova[1], A. Sarsembay[3] and S. A. L. Maftunzada[1,4]

[1]Department of Physics and Technology, Al-Farabi Kazakh National University, Almaty, Kazakhstan
[2]School of Engineering and Applied Sciences, National University of Mongolia, Ulaanbaatar, Mongolia
[3]School-Lyceum №250 named after T.Komekbayev, Karmakchi, Kyzylorda, Kazakhstan
[4]Faryab University, Kārte General Abdul Rashid Dostum Maymana, City Faryab Afghanistan
*e-mail: sarsembaeva.a@kaznu.kz; †odsuren@seas.num.edu.mn

The term 'space weather' refers to adverse conditions on the Sun that could affect the structures of space or terrestrial technology and risk human health or life. Flares produce effects that span the electromagnetic spectrum. During a flash, they emit x-rays and ultraviolet radiation, resulting in extremely high temperatures. The purpose of this work is to create a new algorithm for the identification of solar flares and active regions of the Sun, thus minimizing harm to spacecraft operations in orbit. An algorithm was developed for the automatic detection of active regions of the Sun (sunspots, solar flares), based on methods of image enhancement, segmentation, pattern recognition and mathematical morphology. The sun's surface also displays visible sunspots located in regions of the Sun that are magnetically active and whose number is an indication of the Sun's magnetic activity. In tracking and predicting solar activity, the identification and classification of sunspots are useful techniques. The main objective of this paper is to detect sunspots using images from the Solar Dynamics Observatory.

Key words: solar flares, sunspots, active region.
PACS number(s): 96.60.−j; 96.60.Iv; 96.60.qe

1 Introduction

Sunspots are visible regions of the Sun's photosphere that reflect its activity. The automatic identification of sunspots from digital images is complicated by their shape and variable contrast irregularities and intensity compared to their surroundings. The detection of these sunspots and their characteristics, such as scale, contrast and location on the solar disk, plays an important role in the prediction of space weather and in the study of total solar irradiance, differential rotation, solar convection zone modeling [1], solar radius variability [2-8], and other significant phenomena. For irradiance studies, the area measurements of sunspots are important [9-12]. The measurement of sunspot areas has been shown to rely on the method of detection used and on the images themselves [13-14]. Then, inaccurate calculation of sunspot areas is the key barrier to irradiance modeling [15]. The presence of solar differential rotation is clearly demonstrated by the sunspots. It is easy to see that they are traveling in a few days from east to west on the solar disk. In order to locate sunspots and generate catalogues, many manual or automated methods have been used. Automatic methods use spatial filtering that also affects the resolution of the image and the properties of the sunspot [16-17]. To analyze a small number of images every day, manual methods are sufficient, but automated methods are required to classify these characteristics in recent years as a large and the amount of high-resolution solar images have been obtained from ground and space.The goal of this paper is to identify brightest area of a retinal image using naive and robust methods for the identification of sunspots in solar images.

The goal of this paper is to identify brightest area of a retinal image using naive and robust methods for the identification of sunspots in solar images.

Monitoring of solar flares in a real time is carried out by the Geostationary Operational Environmental Satellite or GOES [8]. Data on the electrons, protons, and X-rays were taken from satellites GOES 13, GOES 14 and GOES 15 [18-19].

On August 9, 2011, on the Sun, X class flares were registered. In total, 8 classes are distinguished in the scale of solar flares: A, B, C, M and X, each subsequent of which exceeds the previous power by 10-100 times. The event, more accurately estimated as X6.9, occurred in the morning and observed for about 20 minutes with a maximum at 08:05 UT [20].

On March 7, 2012 at 00:02 UT, another eruption of solar flare class X5.4 was registered. The event occurred in the active area of 11429 and was observed for about 22 minutes with a maximum at 00:24 UT. In total, 2 solar flares class of X were registered.

On November 5, 2013, around 22:07 on World time there was a fairly strong release of solar matter into space. The solar flare is estimated as X3.3 and its maximum was observed at 22:12 on world time. In total, 1 solar flare of class X were registered.

On February 25, 2014, 4 class C solar flares and 1 class X solar flares were registered. In active area 11990 at 00:39 GMT, solar flare class of X4.9 occurred and was observed for about 10 minutes with a maximum at 00:49 UT.

On September 6, 2017 at 11:53, the X class flare X9.3 was registered. The event occurred in the active area of 12673 and was observed for about 9 minutes with a maximum at 12:02 UT. In total, 2 flares of class X, 3 flares of class M and 2 flare of class C were registered.

Date	X-ray class	Active Region	Start time (hhmm)	End time (hhmm)	Maximim time (hhmm)
2011/08/09	M2.5	11263	03:19	04:08	03:54
	C1.4	11263	07:19	07:27	07:23
	X6.9	11263	07:48	08:08	08:05
	C2.2	11263	13:29	13:57	13:45
	C2.4	11263	15:43	16:04	15:54
	B8.6		16:58	17:05	17:02
	C2.0		18:04	18:42	18:11
	C3.9	11263	23:33	23:49	23:43
2012/03/07	**X5.4**	11429	00:02	00:40	00:24
	X1.3	11430	01:05	01:23	01:14
	C1.6	11429	16:19	16:26	16:22
2013/11/05	C1.6	11889	05:49	06:23	06:02
	M2.5	11890	08:12	08:21	08:18
	C3.5	11885	09:12	09:22	09:18
	C8.0	11890	11:51	12:01	11:58
	C2.5		13:56	14:48	14:22
	C2.3		16:37	16:48	16:42
	C2.3		16:55	17:01	16:59
	C3.1	11890	17:05	17:17	17:15
	M1.0	11890	18:08	18:17	18:13
	C2.1		19:58	20:17	20:07
	C6.9	11890	21:01	21:19	21:13
	X3.3	11890	22:07	22:15	22:12
2014/02/25	**X4.9**	11990	00:39	01:03	00:49
	C5.0	11989	04:27	04:36	04:32
	C4.5	11986	06:16	06:28	06:20
	C5.7	11986	15:04	15:18	15:10
	C2.2	11984	23:31	23:37	23:34
2017/09/06	C1.6	12673	06:17	06:29	06:22
	C2.7	12673	07:29	07:48	07:34
	X2.2	12673	08:57	09:17	09:10
	X9.3	12673	11:53	12:10	12:02
	M2.5	12673	15:51	16:03	15:56
	M1.4	12673	19:21	19:35	19:30
	M1.2		23:33	23:44	23:39

2 Determination of sunspots

Template Matching is a way for a larger image to scan and locate the position of a template image. To this end, OpenCV comes with the cv2. matchTemplate() feature. It simply slides the image of the template over the input image (as in 2D convolution) and compares the template and the input image patch under the image of the template. Several comparison methods are implemented in OpenCV. This returns a grayscale image, where each pixel indicates how much of that pixel's neighborhood matches the template. In the Figure 1 (right panel) shown the brightest pixel location identification in AIA 335 Å wavelengths obtained by using naive and robust methods.

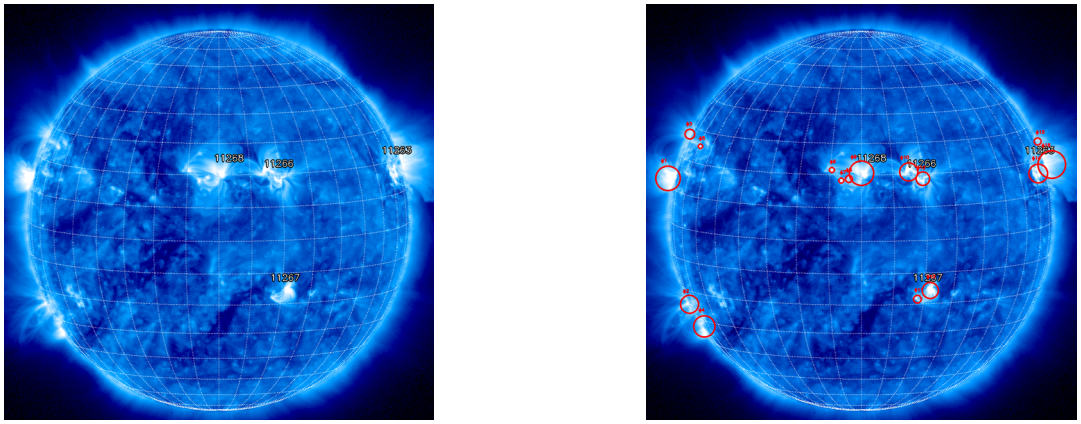

Figure 1 – Detecting the brightest area of a retinal image using naive and robust methods. (2011/08/09, X-ray class: X6.9, AR 1263 in AIA 335 Å)

Using the cv2.minMaxLoc function without any pre-processing is the method of finding the brightest spot in an image. A single argument, which is our grayscale image, is needed for this purpose. This function then takes our grayscale image and, with the smallest and largest intensity values, finds the value of the pixel and (x, y) position, respectively. To break it down: minVal contains the smallest pixel intensity value, maxVal contains the largest pixel intensity value, minLoc specifies the (x, y) coordinates of minVal, and maxLoc specifies the (x, y) coordinates of maxLoc. In this application, we are only concerned with the pixel with the largest value, so we will grab that and draw a circle around the region and display it on. In the Figure 2 (right panel) shown the brightest pixel location identification in AIA 335 Å wavelengths obtained by using naive and robust methods.

The cv2.minMaxLoc function without any pre-processing can leave extremely susceptible to noise. Instead, to eliminate high frequency noise, it is easier first to apply a Gaussian blur to the image. This way, their neighbors will balance out even pixels that have very high values (again, due to noise). From our command line statement, we apply our Gaussian blur with the radius supplied. Then we will call cv2.minMaxLoc again to find the brightest pixel in the picture. Since we have applied a blurring pre-processing phase, however, we have averaged all pixels together with each other's supplied radius. This helps us to suppress high frequency noise and leaves cv2.minMaxLoc significantly less susceptible. We can average over a wider neighborhood of pixels by using a larger radius - thus mimicking larger regions of the image. Additionally, we can sum over smaller regions by using a smaller radius. In the Figure 3 (right panel) shown the brightest pixel location identification in AIA 335 Å wavelengths obtained by using naive and robust methods.

Now, the naive cv2.minMaxLoc method finds this white pixel. The function is working correctly. It is indeed finding the single brightest pixel in the entire image. We are interested in the brightest region of the image, which is the optic nerve center. By utilizing a Gaussian blur, we are able to average a neighborhood of pixels within a given radius, and thus discard the single bright pixel and narrow in on the optic center region without an issue. In the Figure 4 (right panel) shown the brightest pixel location identification in AIA 335 Å wavelengths obtained by using naive and robust methods.

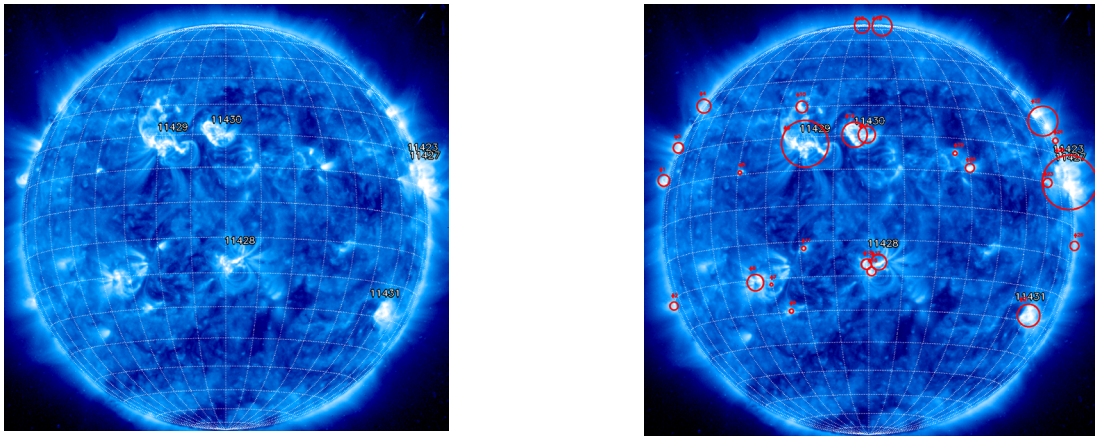

Figure 2 – Detecting the brightest area of a retinal image using naive and robust methods. (2012/03/07, X-ray class: X5.4, AR 1429 in AIA 335 Å)

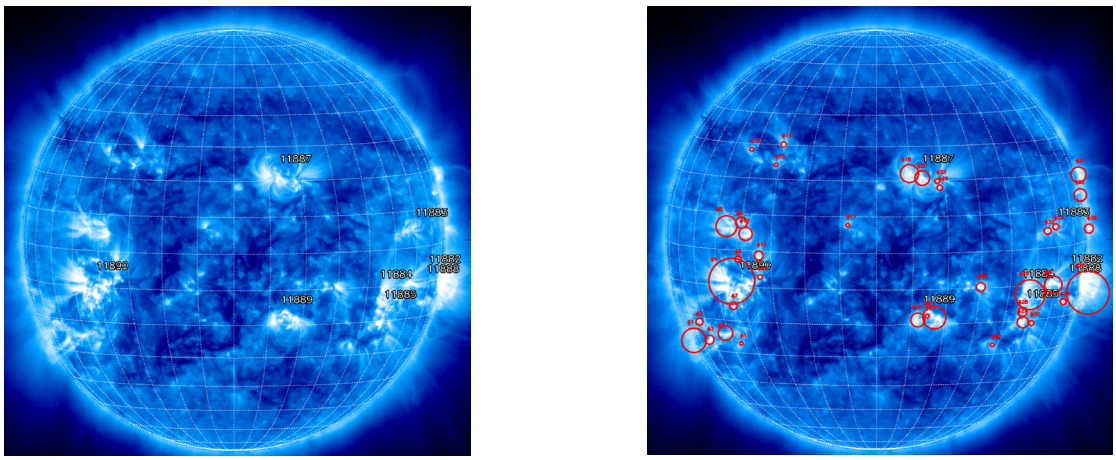

Figure 3 – Detecting the brightest area of a retinal image using naive and robust methods. (2013/11/05, X-ray class: X3.3, AR 1890 in AIA 335 Å)

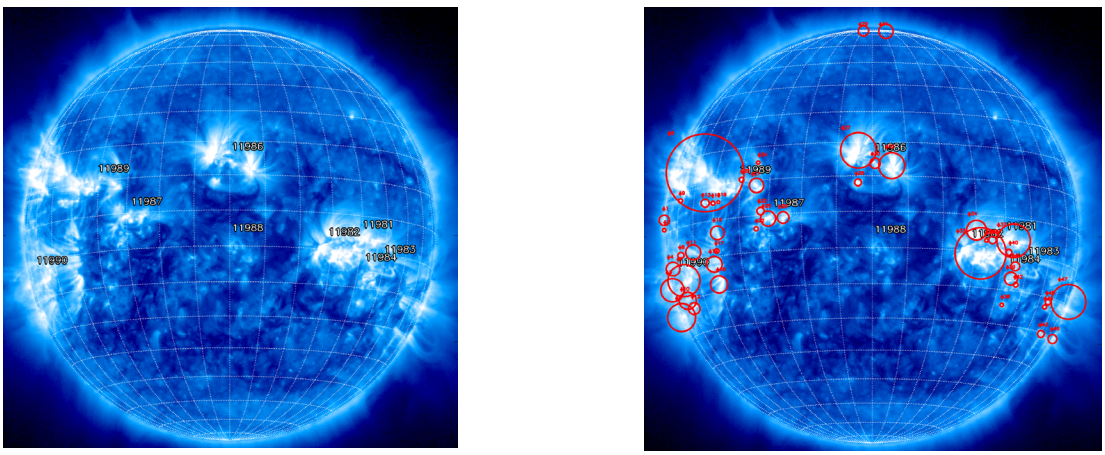

Figure 4 – Detecting the brightest area of a retinal image using naive and robust methods. (2014/02/25, X-ray class: X4.9, AR 1990 in AIA 335 Å)

Obviously, a big aspect of getting the robust method to work correctly is properly setting your radius size. If the radius size is too small, we cannot find larger, brighter regions of the image. However, if we set the radius size too large, then we will detect too large of regions, missing out on the smaller ones, leading to sub-par results. Definitely spend some time playing with the radius size and viewing the results. In the Figure 5 (right panel) shown the brightest pixel location identification in AIA 335 Å wavelengths obtained by using naive and robust methods.

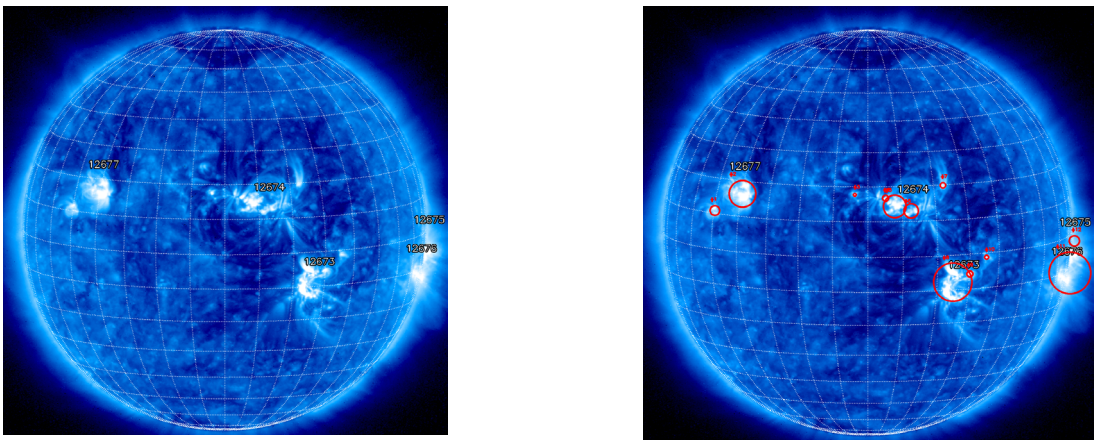

Figure 5 – Detecting the brightest area of a retinal image using naive and robust methods. (2017/09/06, X-ray class: X9.3, AR 2673 in AIA 335 Å)

3 Conclusions

In this work, we applied Gaussian blurring prior to finding the brightest spot in an image. By applying a Gaussian blur, we averaged the pixels within a given radius of each other together. Taking the average allows us to remove high frequency noise. We have used appropriate values for the radius of Gaussian blur. If we take too small of a value, we will mitigate the effects of the average and miss out on the larger, brighter regions. However, if the radius is too large, the small bright regions are not observable.

Acknowledgments

This work was partly supported by the Asian Research Center Foundation for Research program in National University of Mongolia.

References

1 S. Sofia, S. Basu, P. Demarque, L. Li, G. Thuillier. The nonhomologous nature of Solar diameter variations // Astrophys. J. Lett. – 2005. – V.632. – P. L147. https://doi.org/10.1086/498068

2 L. Laclare, C. Delmas, J.P. Coin, A. Irbah. Measurements and variations of the solar diameter // Solar Phys. – 1996. – V.166. –P. 211. https://doi.org/10.1007/BF00149396

3 L. Győri, T. Baranyi, M. Turmon, J.M. Pap. SOHO 11 Symp. From Solar Min to Max: Half a Solar Cycle with SOHO // ESA SP-508. 2002. – P. 203.

4 T. Baranyi, L. Győri, A. Ludmány, H.E. Coffey. Comparison of sunspot area data bases // Mon. Not. Roy. Astron. Soc. – 2001. – V.323. – P.223. https://doi.org/10.1046/j.1365-8711.2001.04195.x

5 C. Fröhlich, J.M. Pap, H.S. Hudson. Improvement of the photometric sunspot index and changes of the disk-integrated sunspot contrast with time // Solar Phys. – 1994. – V.152. – P. 111. https://doi.org/10.1007/978-94-011-0950-5_18

6 S. Zharkov, V. Zharkova, S. Ipson, A. Benkhalil. Technique for automated recognition of sunspots on full-disk solar images // EURASIP J. Appl. Signal Process. 15. – 2005. – P.2573. https://doi.org/10.1155/ASP.2005.2573

7 L. Győri, T. Baranyi, J. Murakozy, A. Ludmány. Comparison of sunspot area data determined from ground-based and space-borne observation // Mem. Soc. Astron. Ital. – 2005. V.76. – P. 985.

8 ftp://ftp.ngdc.noaa.gov/STP/space-weather/solar-data/solar-features/solar-flares/x-rays/goes/

9 http://www.SolarMonitor.org

10 http://www.ngdc.noaa.gov/stp/satellite/goes/

11 A. Sarsembayeva, F. Belisarova, M. Odsuren, A. Sarsembay. February 25, 2014 solar flare data analysis in SunPy // Physical Sciences and Technology. – 2020. – Vol.7 (No. 3-4). – P. 22-26. https://doi.org/10.26577/phst.2020.v7.i2.03

12 M. J. Aschwanden, D. Alexander. Solar flare and CME observations with STEREO/EUVI // Solar Phys. – 2001. – V.204. - P.91. https://doi.org/10.1007/s11207-009-9347-4

13 K. J.H. Phillips, U. Feldman. Properties of cool flare with GOES class B5 to C2 // Astron. Astrophys. – 1995. – V.304. – P.563.

14 H. A. Garcia. Forecasting methods for occurrence and magnitude of proton storms with solar hard X rays // Space Weather. – 2004. – V.2. – P.S06003. https://doi.org/10.1029/2003SW000035

15 Haisch, B., Strong, K.T., Rodono, M. Flares on the Sun and other Stars // Ann. Revs. Astron. Astrophys. – 1991. – V. 29. – P. 275.

16 A. T. Sarsembayeva, A. T. Sarsembay. Solar activity monitoring for the period April 10-20, 2017 // News of the National Academy of Sciences of the Republic of Kazakhstan-series Physico-Mathematical. – 2018. - V.2 (318). - P.9-11.

17 P.L. Bornmann. Limits to derived flare properties using estimates for the background fluxes-Examples from GOES // Astrophys. – 1990. - J.356. – P.733.

18 S.M. White, R.J. Thomas, R.A. Schwartz. Updated expressions for determining temperatures and emission measures from goes soft X-Ray measurements // Solar Physics. – 2005. V.227. – P.231. https://doi.org/10.1007/s11207-005-2445-z

19 N. Gyenge, I. Ballai, T. Baranyi. Statistical study of spatio-temporal distribution of precursor solar flares associated with major flares // Monthly Notices of the Royal Astronomical Society. – 2016. – V. 459 (4). – P. 3532 - 3539. https://doi.org/10.1093/mnras/stw859

20 Švestka Z., Cliver E.W. (1992) History and basic characteristics of eruptive flares. In: Švestka Z., Jackson B.V., Machado M.E. (eds) Eruptive Solar Flares. Lecture Notes in Physics, vol 399. Springer, Berlin, Heidelberg. https://doi.org/10.1007/3-540-55246-4_70

CONTENTS